Paper pa02-075
Submitted to the 28th International Conference on High Energy Physics
ICHEP'96, Warsaw, Poland, July 1996

Charged Particle Multiplicities in Deep Inelastic Scattering at HERA

H1 Collaboration

Abstract

Using the H1 detector at HERA, charged particle multiplicity distributions in deep-inelastic e^+p scattering have been measured over a large kinematical region. The evolution with W and Q^2 of the multiplicity distribution and of the multiplicity moments in pseudorapidity domains of varying size is studied in the current fragmentation region of the hadronic centre-of-mass frame. The results are compared with data from fixed target lepton-nucleon interactions, e^+e^- annihilations and hadron-hadron collisions as well as with expectations from QCD based parton models. Fits to the Negative Binomial and Lognormal distributions are presented.

1 Introduction

The multiplicity distribution of hadrons produced in high-energy interactions is one of the basic measures characterising multiparticle final states. The fluctuation pattern of the number of particles produced in a given domain of phase space reveals the nature of the correlations among the hadrons and is, therefore, sensitive to the dynamics of the process. The multiplicity distribution of charged hadrons has been measured for the full variety of collision processes from e^+e^- annihilations to nucleus-nucleus collisions and the available data cover a wide energy range [1,2]. Numerous theoretical studies have been devoted to the subject [3–5], starting with early investigations by Heisenberg and Fermi [6].

Whereas the total event multiplicity remains of considerable importance, interest has shifted with time towards studies of the multiplicity distribution in subdomains of phase space. In these restricted domains, global conservation constraints are minimised and dynamical correlation effects better revealed [7,8].

In this paper we present results on the multiplicity distribution of charged hadrons produced in the current fragmentation region of deep-inelastic scattering (DIS) e^+p collisions. The analysis is based on data accumulated by the H1 detector at HERA in 1994, corresponding to an integrated luminosity of 1.3 pb^{-1}.

The multiplicity distribution and its moments, fully corrected for detector effects, are studied in the virtual-boson proton (γ^*p) rest system, the hadronic centre-of-mass frame. The measurements are obtained in subdomains of pseudorapidity space[1], both as a function of W, the total hadronic centre-of-mass energy, and Q^2, the negative four-momentum transfer squared in the DIS process. Results from deep-inelastic e^+p interactions from the HERA collider on the charged multiplicity distribution [9] and on the mean multiplicity in the current region of the Breit-frame [10] have already been published.

Here, H1 results are compared with those obtained in DIS fixed target experiments at much lower energy, with hadroproduction in e^+e^- annihilation reactions, with data from hadron-hadron collisions as well as with the expectations of QCD based parton shower models and other more phenomenological approaches.

2 Definitions and phenomenology

2.1 Correlations

The set of probabilities P_n for various numbers of charged hadrons (n) to be produced in a given region of phase space is known as the multiplicity distribution. The continued interest in multiplicity distributions rests on the observation that fluctuations in "counting statistics" are a direct measure of the strength of correlations among the objects being counted. In high-energy physics, this was first exploited by Mueller [11] in the formulation of the concept of short-range order. Since then, correlations have been extensively used as probes of the interaction and hadronisation dynamics [8].

The connection between the multiplicity distribution and particle correlations is made explicit in the relation between the factorial moment of order q, $\tilde{R}_q$, of the multiplicity distribution in a phase space domain (say, rapidity Δ) and the q-particle inclusive momentum density

[1] Pseudorapidity is defined as $\eta^* = -\ln\tan\frac{\theta}{2}$, with θ the angle between the hadron momentum and the direction of the virtual photon in the γ^*p rest system. The current hemisphere is defined as the region of positive η^*.

$\rho_q(1,2,\ldots,q)$ which for identical particles takes the form [11]:

$$\tilde{R}_q = \sum_0^\infty n(n-1)\ldots(n-q+1)\,P_n = \int_\Delta \cdots \int_\Delta \rho_q(1,2,\ldots,q)\,dy_1\ldots dy_q. \tag{1}$$

The functions ρ_q contain, besides genuine dynamical or kinematical correlations, contributions from "random coincidences" in the region Δ. The latter are eliminated by considering the ("connected") correlation functions $\kappa_q(1,2,\ldots,q)$, familiar from statistical physics. Integrated over a domain of size Δ they define the factorial cumulants (or Mueller moments) $\tilde{K}_q$ of the multiplicity distribution [11]. For the normalised quantities $R_q = \tilde{R}_q / \langle n\rangle^q$ and $K_q = \tilde{K}_q / \langle n\rangle^q$ the following relations hold:

$$K_2 = R_2 - 1, \tag{2}$$
$$K_3 = R_3 - 3R_2 + 2; \tag{3}$$

where $\langle n\rangle$ is the mean multiplicity in Δ.

2.2 Scaling

Koba, Nielsen and Olesen (KNO) [12] have studied the limit of the multiplicity distribution in full phase space for $n \to \infty$ and $\langle n\rangle \to \infty$ with $z = n/\langle n\rangle$ fixed. In this case one obtains the KNO form

$$\langle n\rangle\, P_n \simeq \Psi(z). \tag{4}$$

The function $\Psi(z)$ was shown to become asymptotically independent of the total energy if Feynman scaling [13] is satisfied. A proper mathematical reformulation of multiplicity scaling for discrete distributions, valid also at finite energies, was later given by Golokhvastov [14] and is known as KNO-G scaling.

Exact KNO scaling implies that, besides $\Psi(z)$, the factorial moments R_q as well as the moments $C_q \equiv \langle n^q\rangle / \langle n\rangle^q$ are energy independent.

Scaling, either in KNO or in KNO-G form, is experimentally well-established [15, 16] for the full phase space and single hemisphere multiplicity distributions in e^+e^- annihilations, in DIS lepton-hadron interactions and in hadron-hadron collisions [17], except at the highest SPS collider energies [18, 19]. This is remarkable since Feynman scaling is strongly violated in all these processes. However, already in 1970, Polyakov [20] derived the KNO scaling law for e^+e^- hadronic final states within a broad class of field theories. This pre-QCD model is based on a conformal invariance principle which can be reformulated in terms of a scale-invariant stochastic branching process. An energy-independent coupling constant is assumed and the mean multiplicity rises as a power of the energy. The Polyakov derivation, and subsequent work [20], demonstrates that KNO-scaling should hold at least approximately in any model based on similar principles.

2.3 Parametric models

A much studied distribution is the Negative Binomial Distribution (NBD) defined as

$$P_n(k,\overline{n}) = \frac{k(k+1)\cdots(k+n-1)}{n!}\left(\frac{\overline{n}}{\overline{n}+k}\right)^n \left(\frac{k}{\overline{n}+k}\right)^k, \tag{5}$$

with parameters k (or $1/k$) and $\overline{n}$. The average $\langle n\rangle$ and the dispersion D of the NBD are related to the two parameters by

$$\langle n\rangle = \overline{n} \ \ ; \ \ \frac{D^2}{\langle n\rangle^2} = \frac{1}{\overline{n}} + \frac{1}{k}. \tag{6}$$

For $1/k \to 0$ (5) reduces to a Poissonian. $\overline{n}$. The parameter $1/k$ is equal to the integrated second-order correlation function K_2 in the studied phase space domain.

Many phenomenological models for hadroproduction predict multiplicity distributions of a Negative Binomial form. They are reviewed in [3, 21]. In QCD, the NBD is obtained as a solution in Leading-Log Approximation for the gluon multiplicity distribution in a quark jet [22]. Within the framework of the Modified Leading-Log Approximation (MLLA) and Local Parton-Hadron Duality (LPHD) [23], the lower-order factorial moments behave approximately as those of the NBD [24–26].

It is well-established experimentally in a large variety of collision processes that multiplicity distributions, in full phase space as well as in restricted phase space domains, are approximately of Negative Binomial form. However, deviations are observed in high-statistics e^+e^- experiments for final states with hard jets [27, 28] and in hadron-hadron interactions [19]. In fixed target DIS lepton-hadron and lepton-nucleus collisions the NBD adequately describes the multiplicity distributions in the full phase space, in limited (pseudo-)rapidity intervals, as well as in the full current and target hemispheres [2, 29].

A multiplicity distribution exhibiting explicit KNO-G scaling has recently been derived by assuming a scale-invariant bi-variate *multiplicative* branching mechanism as the basis of multihadron production [16]. Application of the central limit theorem leads to a scaling function Ψ of Lognormal form. In this model the multiplicity distribution P_n is related to a continuous probability density $f(\tilde{n})$ and defined as $P_n = \int_n^{n+1} f(\tilde{n})d\tilde{n}$, where $f(\tilde{n})$ is the Lognormal distribution (LND). The mean continuous multiplicity $\langle\tilde{n}\rangle$ is approximately given by $\langle\tilde{n}\rangle = \langle n\rangle + 0.5$. Following [16] one finds

$$P_n = \int_{n/\langle\tilde{n}\rangle}^{(n+1)/\langle\tilde{n}\rangle} \frac{N}{\sqrt{2\pi}\sigma}\,\frac{1}{\tilde{z}+c}\,\exp\left(-\frac{[\ln(\tilde{z}+c)-\mu]^2}{2\sigma^2}\right)\,d\tilde{z}. \tag{7}$$

The integrand in (7) defines the Lognormal scaling function in KNO-G form. It depends on two parameters. Here, $\tilde{z} = \tilde{n}/\langle\tilde{n}\rangle$ is the scaled continuous multiplicity; N, σ, μ and c are parameters of which only two are independent due to normalisation conditions. In fits to data, correlations between the parameters are reduced if d and c are used as free parameters. In terms of σ^2 and μ these are given by

$$\sigma = \sqrt{\ln\left[\left(\frac{d}{1+c}\right)^2 + 1\right]} \ \text{ and } \ \mu = \ln(c+1) - \sigma^2/2. \tag{8}$$

The parameter d is equal to the dispersion of the scaling function. The expression for P_n also depends on $\langle\tilde{n}\rangle$ or $\langle n\rangle$. The latter fit parameter is denoted by m in Table **??**. Exact scaling implies that d and c are energy independent. In addition, the generalised dispersions $D_q = [\langle(n-\langle n\rangle)^q\rangle]^{1/q}$ ($D \equiv D_2$) satisfy a generalised Wróblewski relation [30]. Finally, the mean continuous multiplicity is found to grow as a power of the energy. Comparisons of the Lognormal distribution with data from e^+e^- annihilation, $\nu(\overline{\nu})p$ and $p\bar{p}$ collisions can be found in [28, 16, 31–33].

3 Experimental procedure

3.1 The experiment

The experiment was carried out with the H1 detector [34] at the HERA storage ring at DESY. The data were collected during the 1994 running period when positrons, with an incident energy of 27.5 GeV, collided with protons with an energy of 820 GeV. The following briefly describes the detector components most relevant to this analysis.

The energy of the scattered positrons is measured with a liquid argon (LAr) calorimeter and a "backward" electromagnetic lead-scintillator calorimeter (BEMC). The LAr calorimeter [35] extends over the polar angular range $4^\circ < \theta < 153^\circ$ with full azimuthal coverage, where θ is defined with respect to the proton beam direction (positive z axis). It consists of an electromagnetic section with lead absorbers and a hadronic section with steel absorbers.

The BEMC covers the polar angular range $151^\circ < \theta < 174.5^\circ$. A principal task of the BEMC is to trigger on and measure scattered positrons in DIS processes with Q^2 values ranging from 5 to 100 GeV^2. The BEMC energy scale for positrons is known to an accuracy of 1%.

The central tracking detectors are a hybrid of inner and outer cylindrical jet chambers (CJC1 and CJC2), z-drift chambers and proportional chambers. The latter provide a fast signal and allow H1 to trigger on tracks which originate from the z range expected for e^+p collisions.

The jet chambers, mounted concentrically around the beam line, provide particle charge and momentum measurements from track curvature and cover the angular interval $15^\circ < \theta < 165^\circ$. Up to 56 space points can be measured for non-curling tracks.

The calorimeters and central trackers are surrounded by a superconducting solenoid providing a uniform magnetic field of 1.15 T parallel to the beam axis in the tracking region.

A backward proportional chamber (BPC), situated immediately in front of the BEMC and with an angular acceptance of $155.5^\circ < \theta < 174.5^\circ$, serves to measure the impact point of the scattered positron and to confirm that the particle entering the BEMC is charged. Using information from the BPC, the BEMC and the reconstructed event vertex, the polar angle of the scattered positron can be determined to better than 1 mrad.

Behind the BEMC is a time-of-flight system with a time resolution of about 1 ns. This enables rejection of background events from interactions of protons in the material upstream of the H1 detector.

Positrons and photons emitted at very small angles to the positron beam direction are detected in two electromagnetic calorimeters located at 33 m and 103 m from the interaction point in the positron direction. Designed to measure luminosity by detecting $e\gamma$ coincidences from quasi-elastic radiative e^+p collisions, they are in addition used for studies of background arising from photoproduction.

3.2 Event and track selection

In this analysis two event samples are considered. The "low-Q^2" sample consists of events in which the scattered positron is detected in the BEMC and is limited to a range in Q^2 from 10 to 80 GeV^2. The events of the "high-Q^2" sample have a positron detected in the LAr calorimeter and have $Q^2 > 200$ GeV^2. The event kinematics are reconstructed using the "lepton-only" method based on information from the reconstructed positron and the event vertex.

Neutral current DIS events are selected by demanding a well-reconstructed scattered positron with an energy larger than 12 GeV. This ensures that the remaining photoproduction background comprises less than 1% of the DIS data sample.

Various other sources of background are further reduced by appropriate selections. To exclude events with large QED radiative effects and to ensure substantial hadronic energy flow in the detector, the invariant mass squared, W^2, of the hadronic system, determined from energy clusters in the calorimeter, is required to be larger than 3000 GeV^2.

For comparisons with e^+e^- annihilation and non-single-diffractive data in hadron-hadron collisions, so-called "rapidity-gap" events [36] are removed from the event sample. To that end, events for which the energy deposited within the polar angular range $4.4° < \theta < 15°$ is lower than 0.5 GeV are excluded. The same selection is applied to the various Monte Carlo generated event samples used in the analysis.

An event vertex, reconstructed from tracks in the Central Tracker and located within ± 30 cm of the mean vertex z position, is required to reject beam-induced background and to permit a reliable determination of the kinematic variables. Remaining background is rejected by requiring no veto from the time of flight system.

For this analysis, only charged particle tracks in the Central Tracker are used, after rejection of a possible positron track. Tracks are required to originate from the primary vertex and to lie within the polar angular range $15° < \theta < 155°$. The higher limit eliminates the scattered positron in the low-Q^2 sample. In the high-Q^2 data the positron track is identified with a track-cluster linking algorithm.

With the above selection the overall efficiency for finding a genuine primary track is better than 95%. This estimate is based on Monte Carlo simulations and cross-checked in a visual scan of real and simulated events. From this scan we further conclude that the tracker efficiency is simulated to an accuracy of better than 2%.

The contamination of genuine primary tracks by tracks that have been fitted to the primary vertex, but originate from decay products of short-lived particles, from secondary interactions and from photon conversions, is estimated to be 10%, $< 1\%$ and $\sim 1\%$, respectively. No spurious tracks due to noise hits have been found.

To investigate the sensitivity of our results to the track selection the analysis has been repeated after changing various track-quality criteria, such as the number of hits per track, the cuts on minimal radial track length, the position in the CJC of the first measured point of a track, the minimum laboratory transverse momentum and the maximum distance of closest approach to the event vertex in the transverse plane. The results reported below are found to be stable against all these variations. Residual differences are included in the systematic uncertainties, further discussed in Sect. 3.5.

Within the considered kinematical regions, 53109 low-Q^2 and 1576 high-Q^2 events satisfied the above selection criteria, corresponding to a total integrated luminosity of 1.3 pb^{-1}. The characteristics of the various event samples retained for further analysis are detailed in Table **??**.

3.3 Models for hadronic final states

The hadronic final state of neutral current DIS events is modelled using several Monte Carlo event generators.

The event sample labelled as "DJANGO 6.0" has been generated with the DJANGO program [37]. It is based on HERACLES [38] for the electroweak interaction and on the LEPTO program [39] to model the hadronic final state. HERACLES includes first-order radiative QED corrections and the simulation of real Bremsstrahlung photons. The structure functions used are based on the GRV parameterisation [40] and describe the HERA F_2 results well. LEPTO is used with the colour dipole model as implemented in ARIADNE [41] to model QCD parton cascades. The hadronisation phase is modelled with JETSET [42] and is based on string fragmentation [43].

The sample hereafter labelled as "MEPS 6.4" has also been generated with LEPTO but differs in the treatment of the parton cascade by using first-order matrix elements and leading-log parton showers. It does not include initial- or final-state QED radiation. For the determination of systematic errors connected with the topology of the hadronic final state earlier versions of the MEPS generator as well as HERWIG [44] have been used.

For the events generated with the models listed, the detector response was simulated using a program based on the GEANT [45] package. The detector simulation has been checked by comparing in detail distributions of track quality estimators with the data.

The DJANGO 6.0 sample, comprising nearly 120K events after all selections, is used here for data correction and to unfold the raw multiplicity distributions. The other Monte Carlo generated samples serve to cross-check the multiplicity unfolding procedure and to determine systematic uncertainties.

3.4 Data correction

The raw multiplicity distribution in a given region of (W, Q^2) and pseudorapidity needs to be corrected for several effects. These include loss of events and particles due to limited geometrical acceptance and resolution of the tracking system, limited track-finding efficiency, contamination by tracks from particle decays and interactions in the material of the detector which are assigned to the primary vertex, and also QED initial-state radiation which affects the event kinematics. The results presented in Sect. 4 are corrected for all the above-mentioned effects using the DJANGO 6.0 event sample.

Correction factors are obtained from Monte Carlo simulation by comparing the "true" generated distributions before the detector simulation with the "observed" distributions after this simulation followed by the same reconstruction, selection and analysis as the real data. The "true" distributions do not include the charged decay products of K^0_S, Λ, $\overline{\Lambda}$ and from weakly decaying particles with lifetime larger than $8 \cdot 10^{-9}$ s.

The multiplicity unfolding method used here is similar to that first employed by TASSO [46] and subsequently adopted in various other analyses [9, 27, 31, 47]. Let $T^{MC}_{true}(m)$ be the "true" number of events produced by the Monte Carlo generator with "true" primary charged hadron multiplicity m, and $R^{MC}_{true}(m)$ the number of events with "true" multiplicity m observed after full detector simulation, kinematical reconstruction and event selection. The number of events with m generated tracks and n tracks accepted after simulation and track selection, divided by the total number of events observed with n accepted tracks, $R^{MC}_{rec}(n)$, determines a response matrix with elements $A(m,n)$. The element $A(m,n)$ is the fraction of observed events with n accepted tracks that had "true" multiplicity m. The observed multiplicity distribution $R^{data}_{rec}(n)$ and the "true" multiplicity distribution $T^{data}_{true}(m)$ are then related by

$$T^{data}_{true}(m) = \frac{T^{MC}_{true}(m)}{R^{MC}_{true}(m)} \sum_n A(m,n)\, R^{data}_{rec}(n). \tag{9}$$

The first factor at the right-hand side of (9) corrects for any complete loss of events caused e.g. by inefficiencies and migration outside the investigated kinematical region due to inaccurate reconstruction of the event kinematics.

The underlying assumption of the method is that the relative frequencies occurring in the response matrix derived from the Monte Carlo generator are the same as in the real data. Otherwise, the unfolded multiplicity distribution will be biased towards the generator input distribution. To reduce this bias it has been found necessary to use an iterative procedure whereby the predicted multiplicity distribution at the generator level is reweighted using a previous approximation of the unfolded data multiplicity, until convergence is reached[2]. This is illustrated in Fig. ?? which shows the raw multiplicity distributions in the interval $1 < \eta^* < 5$ for intervals in W in a linear (upper figures) and logarithmic scale (lower figures). The dotted histograms are results from the DJANGO program after detector simulation and deviate appreciably from the real data. The result of the iterative reweighting method is shown as the solid histogram and reproduces the data very well.

As a cross-check of the measurement of the means and dispersions of the distributions obtained by the matrix method, and to allow the study of certain multiplicity distributions given in parametric form, a second method is used. Instead of correcting the observed multiplicity distribution, a theoretical distribution $T^{th}_{true}(m, \vec{a})$, depending on the parameter set $\vec{a}$, is transformed into a raw reconstructed distribution taking all detector effects into account. The function $T^{th}_{true}(m, \vec{a})$ represents the true multiplicity distribution for ideal non-radiative deep-inelastic collisions. The transformed distribution $R^{th}_{rec}(n)$ is then compared to the measured one and the parameters $\vec{a}$ determined with a standard minimum-χ^2 procedure.

A more detailed discussion of the merits and limitations of this method is given in [29, 48]. In the present paper it is used to make comparisons with the Negative Binomial and Lognormal distributions.

3.5 Systematic errors

In this section we discuss various sources of possible systematic uncertainties. Each possible systematic effect is independently varied and the analysis repeated as outlined in the previous section. The difference in the final result, relative to the quoted result based on DJANGO 6.0, is taken as one contribution to the systematic uncertainty. The errors from all sources are added in quadrature.

For illustration, the change in the mean charged multiplicity due to various effects are summarised in Table ??. Results are given for both the full current hemisphere ($\eta^* > 0$) where the corrections are largest and the pseudorapidity range $1 < \eta^* < 3$, where the detector acceptance is high.

- Photoproduction events that survive the DIS selection will have a fake positron detected in the BEMC. Above a reconstructed scattered lepton energy E'_e of 14 GeV the contribution of photoproduction events is practically zero. For $12 < E'_e < 14$ GeV the background contribution is estimated to be 5% [49]. This means that photoproduction events only contribute in the highest W interval. To exclude events in this interval the E'_e cut is raised from 12 to 14 GeV, a smaller radial extension of the BEMC energy cluster is demanded and events with a positron detected in the electron tagger are rejected. This results, however, in a negligible change of the mean multiplicity in the highest W interval.

- The BEMC energy scale is known to an accuracy of 1%. Decreasing the energy scale by its error reduces the mean multiplicity by a maximum of $\sim 3\%$.

[2]Convergence was reached in all kinematical regions after 3 iterations, at the most.

- The track selection criteria ensure a high efficiency (above 95% inside the acceptance region). To restrict tracks to a region of even higher efficiency additional kinematical selections are introduced. The polar angle θ of a track is required to be larger than 22° and the transverse momentum p_T to be larger than 0.15 GeV/c. After correction, this decreases the mean multiplicity in the full current hemisphere by about 2%. However, exclusion of tracks from the forward Central Tracker region or with low p_T enhances the sensitivity to the type of Monte Carlo generator used. The contribution to the total systematic error is, therefore, estimated by applying additional selections on the track *quality*, requiring more than 10 hits, a track length of more than 10 cm and a start point in CJC1. With these selections, the fraction of tracks for which track segments in the inner and outer CJC are not linked, and therefore double-counted, is kept below 0.3% and reproduced by the Monte Carlo simulation within 30%.

- The multiplicity unfolding is performed iteratively to reduce the dependence on the generated Monte Carlo multiplicity distribution. To estimate the importance of any residual systematic bias on the mean and dispersion of the multiplicity distribution, a Negative Binomial distribution, smeared for detector effects, is fitted to the reconstructed data multiplicity distribution. The effect on the determination of the mean multiplicity is well below 2%. In addition, $\langle n \rangle$ has been estimated from the fully corrected single-inclusive charged particle η^* spectrum in each W-interval, using the standard bin-by-bin correction method. The (generally small) difference between extremes is taken as one contribution to the overall systematic error.

- The predictions of the Monte Carlo generators used here differ significantly in the pseudorapidity domain $0 < \eta^* < 1$. This region lies partly outside the Central Tracker acceptance at low W. Since a change in generator multiplicity outside the acceptance region does not affect the reconstructed distribution, a generator dependent bias cannot be removed by reweighting the input distribution. A systematic uncertainty has been assigned to the results pertaining to the full current hemisphere ($\eta^* > 0$) by taking the maximum difference between results derived from different event generators. Table 2 illustrates the maximum size of the effect obtained from the generator LEPTO 6.1.

The contribution from decay products of K_S^0, Λ, $\bar{\Lambda}$ etc is subtracted via the unfolding procedure. However, recent studies at HERA indicate that the K_S^0 production rate may be overestimated by about 10% [50] in the models used for correction. Such a difference leads to a systematic underestimation of the mean multiplicity of at most 0.4%.

From event simulation it is estimated that about 0.1 tracks per event assigned to the primary vertex are, in fact, due to photon conversions in the detector material. To account for possible differences between the event simulation and the real detector response an additional 1% systematic error on the mean multiplicity is assumed.

4 Results

The multiplicity distribution has been measured, in the kinematic regions in W and Q^2 listed in Table 1, for charged particles with pseudorapidity in the domains $1 \leq \eta^* \leq \eta_c^*$ with $\eta_c^* = 2, 3, 4, 5$ and in intervals of unit pseudorapidity centered at $\eta^* = 2.5, 3.5, 4.5$, as well as for the full current hemisphere defined as the domain $\eta^* > 0$. The data are integrated over particle centre-of-mass transverse momentum to allow comparison with other experiments.

The corrected multiplicity distributions, in four W intervals and four η^* domains, are given in Table 3. For each multiplicity, n, the relative frequency, P_n, the statistical uncertainty (first) and the systematic uncertainty (second) are given. The statistical uncertainties take into account the finite number of events in the data and in the generated samples. They are calculated by means of a Monte Carlo sampling procedure which ensures propagation of sampling fluctuations and statistical correlations into the statistical error of the measurement. The same technique is employed to determine statistical errors on moments of the multiplicity distribution and other derived quantities. It must be noted that the P_n values given in the table are correlated for nearby values of n due to the method of correction.

Table 4 summarises corrected results in various pseudorapidity domains for the mean charged multiplicity $\langle n \rangle$, the generalised dispersions D_q, the normalised multiplicity moments C_q ($q = 2, 3, 4$) and the factorial moments R_2, R_3. The table also lists values for the third-order factorial cumulant K_3 for those intervals where a statistically significant measurement is possible.

Estimates of the first two moments (i.e. $\langle n \rangle$ and D) of each multiplicity distribution have also been obtained using the parametric method, described in Sect. 3.4, based on fits of the Negative Binomial and Lognormal distributions. The results from this method and from the matrix unfolding are found to be consistent.

Not all of the statistical moments listed in Table 4 will be discussed in detail. They have been measured in many experiments and are included for reference purposes.

4.1 Current hemisphere multiplicity moments

To allow comparison with lepton-nucleon fixed target data and single-hemisphere data from e^+e^- experiments, we present in this section results on the moments of the charged particle multiplicity distribution in the full current hemisphere $\eta^* > 0$. The limited experimental acceptance in the interval $0 < \eta^* < 1$, in particular for the range $80 < W < 115$ GeV, renders the H1 data in this region more sensitive to the Monte Carlo generators used in the correction procedure than in other pseudorapidity domains. The quoted systematic errors reflect this additional uncertainty[3].

Data on multiplicity distributions in a single hemisphere and in restricted domains of rapidity are available from several e^+e^- experiments [27, 31, 46, 51]. To compare DIS data with that for e^+e^- annihilations we have chosen to use the e^+e^- JETSET parton shower model, with parameter settings as used by the DELPHI collaboration [52]. This model reproduces in detail the multiplicity distributions in the full phase space and in restricted intervals of rapidity [27, 28].

The JETSET e^+e^- predictions presented below (labelled as "JETSET e^+e^-" in the figures) are obtained for a mixture of "primary" light quark pairs only. Decays of K^0_S, Λ and $\overline{\Lambda}$ are treated as in the DIS data and in the simulations, thereby avoiding experiment- and energy-dependent corrections to published data[4]. The contribution to $\langle n \rangle$ from charmed quark fragmentation, estimated at LEP to be a factor 1.02 ± 0.03 larger than for light quarks [54] is neglected. The model predictions are also used in domains of pseudorapidity where no direct e^+e^- measurements exist. For these, the conclusions should be treated with caution.

[3] Diffractive events are removed from the H1 DIS sample by rejecting events with a "rapidity gap". *Not* removing these events would result in a 3% decrease of the mean multiplicity. This effect is not included in the quoted systematical errors.

[4] We have verified that the JETSET e^+e^- predictions, with five active flavours, reproduce the published data in the PETRA-LEP energy range, including recent measurements at 130 GeV [53].

4.1.1 Mean Charged Multiplicity

Figure 2a shows the mean charged multiplicity for $\eta^* > 0$, measured by this and other lepton-nucleon experiments [33, 29, 55, 56] as a function of W.

Here and in the following, unless stated otherwise, the total errors are the overall uncertainties computed by adding the statistical and systematic errors in quadrature. When two error bars are displayed the inner error bar is the statistical error and the outer one is the total error. For data from other experiments we have used the published systematic errors, whenever available. Otherwise a systematic error of 5% is assumed.

In the W-range covered by HERA, $\langle n \rangle$ is compatible with a linear increase with $\ln W$. Combined with the data at lower energy[5] it is evident, however, that the mean multiplicity increases faster than $\ln W$. The HERA data confirm, for the first time in DIS lepton-proton scattering, the faster-than-linear growth of $\langle n \rangle$ with $\ln W$, a feature already well-known from e^+e^- annihilations and hadron-hadron collisions, and expected in perturbative QCD.

Various models predict the evolution of the mean multiplicity with energy. We have fitted[6] several parameterisations to the data plotted in Fig. 2a.

According to the KNO-G prescription an appropriate power-law form is, following [16]

$$\langle n \rangle = a \cdot (W/W_0)^{2b} - c, \qquad (10)$$

where the constant c may be regarded as a "discreteness correction" with the value $c = 0.5$ and $W_0 = 1$ GeV. The fit yields $a = 1.40 \pm 0.04$, $b = 0.20 \pm 0.01$ with $\chi^2/\mathrm{NDF} = 39/23$. The value for the power b agrees with that obtained by Szwed *et al.* ($b = 0.221$) in a comprehensive analysis of the *full* phase space multiplicity distribution in e^+e^- annihilation [16].

We have further compared the DIS data to the Modified Leading-Log (MMLA+LPHD) prediction [57] in the form proposed in [58] and valid for running QCD coupling α_s:

$$\langle n \rangle = c_1 \, \frac{4}{9} \, N_{LA} + c_2, \qquad (11)$$

with

$$N_{LA}(Y) = \Gamma(B) \left(\frac{z}{2}\right)^{1-B} I_{1+B}(z), \qquad (12)$$

where $z \equiv \sqrt{\frac{48}{b}Y}$, with $Y = \ln(W/2Q_0)$, $a = 11 + 2N_f/27$, $\beta_0 = 11 - (2/3)N_f$, $B = a/\beta_0$ and N_f the number of active flavours; I_ν is a modified Bessel function of order ν and Γ is the Gamma function.

In [58] this expression was shown to describe the mean charged multiplicity in e^+e^- annihilation from LEP energies down to centre-of-mass energies of 3 GeV. The factor $\frac{4}{9}$ accounts for the multiplicity difference in a quark and gluon jet; c_1 is a (non-perturbative) normalisation parameter and c_2 the "leading parton" contribution, not included in the theoretical calculation. Using the same shower cut-off value $Q_0 = 270$ MeV and $N_f = 3$ as in [58], we find $c_1 = 1.21 \pm 0.05$, $c_2 = 0.81 \pm 0.08$ with $\chi^2/\mathrm{NDF} = 45/23$. The best-fit curve is shown in Fig. 2a (dashed line) and describes the data over a wide W-range.

[5] For clarity, only a representative sample of νp data is plotted.

[6] Because of the systematic difference between the EMC and E665 results, discussed in [29], fits are performed *without* the E665 data points. The errors on best-fit parameters quoted in this section include systematic uncertainties.

The mean multiplicity has also been computed as a function of $\alpha_s(W)$ including the resummation of leading and next-to-leading corrections [59] with the result

$$\langle n \rangle = a\, \alpha_s^b \exp\left(c/\sqrt{\alpha_s}\right)\, [1 + d \cdot \sqrt{\alpha_s}]\,, \tag{13}$$

where the parameter a cannot be calculated from QCD. The constants b and c are predicted by theory[7]. This QCD prediction has been successfully tested over a wide energy range in several analyses of the mean charged multiplicity in e^+e^- annihilation [31,32,27,47], including the recent LEP measurement at 130 GeV [53]. For the running coupling constant we use the two-loop expression :

$$\frac{\alpha_s(W^2)}{4\pi} = \frac{1}{\beta_0 \ln(W^2/\Lambda^2)} - \frac{\beta_1 \ln\ln(W^2/\Lambda^2)}{\beta_0^3 \ln^2(W^2/\Lambda^2)}, \tag{14}$$

with the constant β_0 as defined before, $\beta_1 = 102 - 38N_f/3$, $b = 1/4 + (10N_f)/(27\beta_0)$ and $c = \sqrt{96\pi}/\beta_0$. According to [59] Λ needs not be identical to $\Lambda_{\overline{\rm MS}}$, although both are expected to be rather similar, in particular if the $\mathrm{O}(\sqrt{\alpha_s})$ correction turns out to be small.

A fit of the data to the form (13) with a and d as free parameters, $\Lambda = 263$ MeV [60] and $N_f = 3$ yields $a = 0.041 \pm 0.006$ and $d = 0.2 \pm 0.3$ with $\chi^2/\mathrm{NDF} = 27/23$.

The functions (10), (11) and (13) are fairly similar[8] and clear differences between them will become visible only at much larger energies.

The above comparisons confirm and extend earlier indications from μp interactions [61] that the rate of increase with energy of $\langle n \rangle$ in the current fragmentation region of DIS lepton-nucleon interactions is similar to that observed in e^+e^- annihilation in the presently covered energy range.

The energy evolution of the mean multiplicity of partons emitted from a primary parton has been calculated for running as well as for fixed α_s [57,62]. In the latter case the multiplicity rises as a power of the energy as in equation (10). For running coupling the growth is slower than any power of W, but faster than any power of $\ln W$, as in equations (11) and (13).

The various parameterisations discussed here show that, up to present energies, distinction between fixed and running α_s, based on measurements of $\langle n \rangle$, is still not possible. The data are sensitive, however, to soft gluon interference in QCD. Neglecting interference would increase the multiplicity anomalous dimension [57], $\gamma = \mathrm{d}\ln\langle n \rangle/\mathrm{d}\ln W^2$, by a factor $\sqrt{2}$. This has been shown [62] to be inconsistent with data for any reasonable value of Λ and confirmed for DIS in [9,10].

In a strict sense the perturbative QCD results apply only to the soft component of the parton cascade emitted by a single quark or gluon jet. They are approximately valid for initial parton configurations such as those encountered in e^+e^- annihilation and in the simple quark-parton picture of DIS. However, the dynamics of DIS processes is more complex than in e^+e^- and differences of detail are to be expected [63].

In Fig. 2a we compare the DIS multiplicity with single-hemisphere results as expected from the JETSET generator in e^+e^- annihilation for light quark-antiquark pairs (dotted line)[9]. The evolution with energy of $\langle n \rangle$ in e^+e^- is similar to that in DIS. The H1 results are consistent with the presence of a small multiplicity excess in e^+e^- annihilation, relative to DIS, above

[7] Note that formula (12) reduces to (13) at large z.

[8] The corresponding fitted curves practically coincide with the dashed line in Fig. 2a and are not shown for reasons of clarity.

[9] The single hemisphere multiplicity distribution for e^+e^- is calculated relative to the thrust axis.

$W = 10$ GeV, which has been noted before [64, 65]. In measurements of inclusive charged particle spectra at HERA [66, 67] a similar excess is seen near zero longitudinal momentum in the hadronic centre-of-mass. It is usually attributed to more prolific gluon emission in e^+e^-. The MEPS 6.4 generator for DIS at the HERA energy (solid line) overestimates substantially the mean charged multiplicity.

4.1.2 The ratio $\langle n \rangle / D$ and R_2

In Fig. 2b we show the ratio of $\langle n \rangle$ to D in a comparison with fixed-target DIS data. This ratio is expected to be energy independent if KNO-scaling holds. The data above 10 GeV are indeed constant, within large errors, after a clear rise at lower W. The JETSET e^+e^- prediction (dotted curve) exhibits rather similar energy dependence and, moreover, illustrates that KNO-scaling is only approximately valid. The MEPS 6.4 generator (solid line) agrees well with the HERA data.

The normalised second-order factorial moment $R_2 = \langle n(n-1) \rangle / \langle n \rangle^2$ is plotted in Fig. 2c. This quantity is equal to the integrated two-particle inclusive density and is, therefore, a direct measure of the strength of hadron-hadron correlations. It shows little, if any, energy dependence over the HERA range but rises steadily at lower W. The behaviour is very similar for e^+e^- final states. The experimental values of R_2 are further compared with a QCD calculation which, for a quark jet, predicts R_2 to behave as

$$R_2 = \frac{7}{4} \left[1 - \kappa \sqrt{\alpha_s}\right], \tag{15}$$

with $\kappa = 0.88$ for three flavours [24]. Leading and next-to-leading order predictions are plotted, with α_s calculated according to the two-loop formula (14) and the scale parameter set to $\Lambda = 263$ MeV. Both curves are significantly above the data. Nevertheless, it is interesting that the next-to-leading order calculation comes closer to the data, although the disagreement remains considerable. The data are rather well reproduced by the JETSET model in the case of e^+e^- annihilation, a fact confirmed by differential measurements of the two-particle correlation function by OPAL [68]. The prediction of MEPS 6.4 for DIS (solid line) is in agreement with the HERA results.

The results presented in this and the previous section indicate similarities of the low-order moments of the single-hemisphere multiplicity distribution in DIS and e^+e^- annihilation, in conformity with the hypothesis of approximate universality of quark and gluon fragmentation.

QCD predictions for the energy dependence of the mean *parton* multiplicity, derived from analytical solutions of the evolution equations, are in agreement with that observed for *hadrons* and thus add to the existing support for the LPHD *ansatz* at the single-inclusive level. The large disagreement between data and QCD next-to-leading order calculations of [24] for R_2 suggests that extension of the LPHD hypothesis to higher-order inclusive correlations may not be justified [62].

4.2 The multiplicity distribution in pseudorapidity domains

In this section we study the multiplicity distribution and its moments in domains of pseudorapidity, limited to the current fragmentation region $\eta^* > 1$. We examine the Q^2 and W dependence and compare with data from other types of interactions and with predictions from the MEPS 6.4 generator.

4.2.1 Q^2-dependence

In the simple quark-parton model the properties of the total hadronic system produced in a deep-inelastic lepton-hadron collision depend on the lepton kinematical variables Bjorken-x and Q^2 only through the invariant mass W of the hadronic system. In QCD, scaling violation of the quark fragmentation functions and of the parton distributions introduce an explicit Q^2 dependence even at fixed W. Fixed target DIS electron, muon and (anti)neutrino experiments at low energies confirm that the global characteristics of the hadronic final states and the average number of produced hadrons in particular, vary most significantly with W. At fixed W, only weak dependences on Q^2 are observed [2,69]. Such results are in accord with the Bjorken-Kogut correspondence principle [70] and imply that the densities in the hadron plateaux spanning the current, central and target regions are quite similar [70, 71]. Only recently has a statistically significant Q^2 dependence of the mean charged hadron multiplicity been established in μ^+p and $\nu(\overline{\nu})p$ interactions [72, 73]. The effect is limited to a restricted region in Feynman-x: $-0.15 < x_F < 0.15$, where x_F is the fractional longitudinal momentum of a hadron in the hadronic centre-of-mass frame. There are no published results on a possible variation with Q^2 of the *shape* of the multiplicity distribution.

The H1 experiment allows us to investigate the charged particle multiplicity distribution over a widely extended range of Q^2 in a novel energy domain. In Fig. 3 are plotted the mean charged multiplicity and the dispersion of the multiplicity distribution in four intervals of W, and in the pseudorapidity domain $1 < \eta^* < 5$, covering part of the current fragmentation hemisphere. Within errors, no significant variation with Q^2, in a fixed interval of W, is observed for $\langle n \rangle$ and D in the range $10 < Q^2 < 1000$ GeV^2. The solid lines in Fig. 3 are fits to a constant.

To ascertain the evolution with Q^2 seen at much lower energy it will be necessary to study the multiplicity distribution in the central and proton-remnant pseudorapidity regions which are not covered in this analysis. A similar study with quasi-real photons at HERA would be of evident interest.

The data presented in subsequent sections have been obtained from data samples averaged over the full Q^2 region ($Q^2 > 10$ GeV^2) covered by this experiment.

4.2.2 The shape of the multiplicity distribution

In Fig. 4 we show, as a representative example, the multiplicity distribution in the interval $115 < W < 150$ GeV, measured in various η^* domains. In this figure only statistical errors are plotted. The distribution for the widest η^* interval is plotted at its true scale. The distributions for the other intervals are shifted down by multiples of ten.

The figures illustrate that the multiplicity distribution, at fixed W, becomes narrower as the size of the η^* interval is reduced. However, the same distributions plotted in KNO form (not shown) widen under the same conditions. The latter property is in part related to the diminishing influence of global conservation constraints and was first predicted in [7].

Figure 4 also shows the predictions from MEPS 6.4 (open symbols). Significant deviations are noted. The model overestimates the mean multiplicity (cf. Fig. 2a) and, consequently, does not reproduce the small- and high-n tail of the distribution. These defects are seen in all W and η^* intervals examined.

Numerous parameterisations for the shape of the multiplicity distribution are used in the literature. Here we concentrate on the Negative Binomial Distribution (NDB) and the Lognormal Distribution (LND). The phenomenological arguments leading to these forms are discussed in Sect. 2. The parameters of these parametric models are obtained from a least-χ^2 fit to the uncorrected multiplicity distributions, as explained in Sect. 3.4. The best-fit parameters for all studied pseudorapidity and W intervals are summarised in Table **??**. The errors quoted are the quadratic sum of the statistical error and the systematic uncertainties.

The solid (dashed) line in Fig. 4 shows how the LND (NBD) compares to the measurements. Inspection of this figure and of Table **??** indicates that the LND gives a reasonably accurate description of the data, in particular in the smallest η^* domain. However, the quality of the fits deteriorates in larger domains. The NBD fits are acceptable in the smallest η^* domain but become progressively worse for larger intervals. The two distributions are seen to differ most for low multiplicities. Nevertheless, it may be verified from Tables 4 and 5 that the estimates for the mean and dispersion of the multiplicity distribution, derived from these parameterisations, agree very well with those derived from the fully unfolded distribution. Parametric forms, such as the NBD and LND, therefore remain useful for phenomenology.

In intermediate-size rapidity intervals in e^+e^- annihilations at LEP both the LND and the NBD are unable to describe the multiplicity distribution which exhibits a prominent shoulder at intermediate n-values. The shoulder is most prominent in the single-hemisphere distributions [27, 28]. This structure results from a superposition of two-jet and three- or four-jet events. The effect demonstrates that the fluctuations in the number of hadrons, and therefore the multiplicity distribution, carries information on the hard partonic phase of the multihadron production process, even after soft hadronisation. The connection between parton-level and hadron-level dynamics has been investigated by the Lund group for parton cascades treated in the dipole formalism [74,75]. It is shown that, for centre-of-mass energies above ~ 50 GeV, the fluctuations in the *hadron* multiplicity are to better than 90% determined by the hardest and second-hardest gluons emitted. Further softer radiation and subsequent (string-)hadronisation, adds only small (sub-Poissonian) fluctuations to those induced in the initial stage of shower development. These analytical results provide a quantitative realisation of the notion of Local Parton-Hadron Duality derived directly from perturbative QCD.

The H1 measurements show no evidence for a shoulder structure of the type seen in e^+e^-. Neither is such a structure present in the multiplicity distribution predicted by MEPS 6.4. The H1 data, which cover larger W values than presently reachable in e^+e^- annihilation, are in qualitative accord with the QCD expectation that hard multi-jet production is less frequent in lepton-hadron collisions. Radiation from the target remnant—a composite colour source—is expected to be strongly suppressed by the so-called "antenna-effect" [75]. For sufficiently small values of Bjorken-x it also suppresses hard gluon radiation in the current region. The probability per event for hard gluon radiation is consequently larger in e^+e^- annihilation. As shown in [75], the antenna-effect leads to smaller values of the *local* multiplicity anomalous dimensions and to smaller multiplicity fluctuations for DIS in the current region, compared to e^+e^- annihilation. These topics are examined in the following sections.

4.2.3 KNO-scaling and correlations

To demonstrate the energy scaling of the multiplicity distribution in DIS in the energy range opened up by HERA we show in Fig. 5 the KNO distributions $\Psi(z)$ in the domain $1 < \eta^* < 5$ for four intervals in W, plotted on a logarithmic (top) and a linear scale (bottom), respectively. The dotted curve is the KNO-function for e^+e^- annihilation[10] in the same η^*-range, obtained

[10]Single-hemisphere e^+e^- data are known to exhibit KNO-scaling above ≈ 20 GeV [46,31,27]. The JETSET simulations show the same in the domain $1 < \eta^* < 5$ discussed here.

from the JETSET parton shower model at a centre-of-mass energy of 91.2 GeV. The two data sets are remarkably similar.

Exact KNO scaling implies that the function $\Psi(z)$, and hence the moments C_q, are independent of W. Fig. 6 displays the variation of C-moments with W for various η^*-intervals (see also Table 4). At fixed W the moments increase as the η^*-domain decreases in size, reflecting the widening of the multiplicity distribution in KNO-form.

The moments in the smallest and largest pseudorapidity domain show, within errors, little W dependence and thus exhibit approximate KNO-scaling. However, violation of KNO-scaling is seen in intermediate-size intervals. This observation is consistent with the clear KNO-scaling violations observed at HERA in DIS data on multiplicity distributions measured in the current region of the Breit frame of reference [9, 10].

The MEPS 6.4 generator (solid line) describes the data well in the largest η^* domains but tends to underestimate C_2 and C_3 in the smaller ones.

The dotted lines in Fig. 6 are expectations from JETSET for e^+e^- in the same pseudorapidity domains as covered by H1. Large differences between DIS and e^+e^- annihilation are predicted, in particular for higher-order moments in small η^* domains. However, in the largest domains the e^+e^- results join smoothly with the DIS data. It will be of interest to confirm these predictions with future measurements at LEP in the W-range studied here.

Also shown is a measurement for non-single-diffractive $p\bar{p}$ collisions at $\sqrt{s} = 200$ GeV[11] in the interval $1 < |\eta^*| < 2$ from UA5 [19]. Here the fluctuations in particle density number near the central plateau are significantly larger than in DIS. It will, however, be shown in Sect. 4.2.4 that the particle density itself is quite similar in the two processes.

The values of the cumulants K_q in a given domain of phase space are a direct measure of the strength of "genuine" correlations among hadrons. Inspection of Table 4 shows that the three-particle correlation function is significantly different from zero only in the smallest interval $1 < \eta^* < 2$, in accord with measurements for other types of interactions [8].

To study the two-particle correlation function more directly we present in Fig. 7 $\langle n \rangle$ and the second-order factorial moment $R_2 = 1 + K_2$ in η^*-domains. The mean charged multiplicity increases approximately as $\ln W$ for $1 < \eta^* < 2$, i.e. near the central region, but faster in larger domains. The W dependence of R_2 for $1 < \eta^* < 2$ is less clear, in view of the errors, but compatible with the slow (logarithmic) rise well established in hadron-hadron and e^+e^- interactions. The MEPS 6.4 generator reproduces reasonably well the behaviour of R_2 but systematically overestimates the mean multiplicity in all η^* domains.

4.2.4 Particle density and E_T flow

The flow of transverse energy, E_T, in multiparticle final states at high energy is studied intensively at hadron colliders and by the HERA experiments. The E_T distribution in a given phase space domain, and its moments, are convoluted observables. They depend not only on the particle density and the p_T structure of the collisions but also on multiparticle correlations, and, therefore, on the moments of the multiplicity distribution in that domain [76]. Here we compare the evolution with W of the particle density to that of the mean E_T for DIS and hadron-hadron interactions.

Fig. 8 shows a compilation of measurements in DIS [29, 56] and in non-single-diffractive hadron-hadron collisions [19, 77–80] of mean charged multiplicity per unit of rapidity or pseu-

[11] The UA5 measurement at $\sqrt{s} = 900$ GeV (not shown) yields $C_2 = 1.84 \pm 0.02$, $C_3 = 4.0 \pm 0.1$ and $C_4 = 14.5 \pm 0.8$, the same, within errors, as the results at 200 GeV.

dorapidity (solid symbols). The H1 data are the same as those shown in Fig. 7a. The open symbols show measurements of the mean E_T in the region $-0.5 < \eta^* < 0.5$, presented and discussed in [81]. The solid line shows a parameterisation used by UA1 [80] with the form $\langle n \rangle = 0.35 + 0.74\,(W^2)^{0.105}$.

In spite of the differences in the rapidity region covered, the known difference between pseudorapidity and rapidity density, different experimental procedures and systematics, it remains of interest to note that the charged particle density for DIS at HERA interpolates quite smoothly with DIS and hadron-hadron data at lower and much higher energy. This observation is consistent with the analogy between virtual photon-hadron, real photon-hadron and hadron-hadron interactions originally advocated by Gribov and Feynman[12], which suggests universality of dynamics in the central plateau [81]. However, the difference in correlation strength, noted in the previous section, suggests that such "universality", while applicable to single-inclusive spectra [81], may not hold for higher-order correlations.

Several mechanisms have been suggested to explain the dynamics of the large multiplicity fluctuations in soft hadron-hadron collisions: impact-parameter averaged Poisson-like fluctuations; multiple soft parton interactions in the same event leading to mini-jets [82]; multi-pomeron exchange as in the Dual Parton Model [83] and multi-string configurations as in the Lund FRITIOF model [84]. These mechanisms have no direct analogues in DIS, except for the boson-gluon fusion QCD process which can lead to two-string colour topologies and could, therefore, mimic multi-string properties in hadron-hadron models.

In Fig. 8 we further compare the energy evolution of $\langle n \rangle$ in the central region in DIS with that in e^+e^- annihilation. The dotted curve is the prediction from the JETSET generator for the interval $1 < \eta^* < 2$. It shows that the hadron density evolves much faster with W than in the DIS and hadron-hadron data.

The energy evolution of $\langle n \rangle$ in perturbative QCD is controlled by the anomalous multiplicity dimension γ through $\gamma = \mathrm{d}\ln\langle n \rangle / \mathrm{d}\ln W^2$. For e^+e^- annihilation, and in restricted (pseudo)rapidity intervals, it is given by $\gamma_{ee}(\eta^*) \sim \sqrt{3\alpha_s(k_{Tmax}^2)/2\pi}$, where k_{Tmax} is the maximum possible transverse momentum at a given η^* [75]. From the JETSET e^+e^- predictions above $W = 20$ GeV we derive that γ_{ee} is constant with a value of 0.16. This is somewhat smaller than expected from the analytic result (~ 0.22 at 200 GeV) but agrees with that quoted in [75].

In leptoproduction, where gluon emission from the nucleon remnant is thought to be suppressed, $\gamma_{DIS}(\eta^*)$ depends more strongly on η^* with $\gamma_{DIS}(\eta^*) \sim (1/2)\gamma_{ee}(\eta^*)$ for not too large positive η^* [75]. From the DIS data in Fig. 8, using the UA1 parameterisation, we estimate $\gamma_{DIS} = 0.8 - 0.9$, consistent with expectations. This is the first semi-quantitative experimental confirmation of the "antenna suppression" effect in DIS. However, better data are needed, also at lower W, to exploit these perturbative QCD predictions in a fully quantitative manner. This result also implies that the rate of increase with energy of $\langle n \rangle$ in the full current hemisphere for DIS and that in a single hemisphere for e^+e^- annihilations, discussed in Sect. 4.1.1, are expected to differ at higher centre of mass energies.

Non-asymptotic analytical QCD predictions for higher-order multiplicity moments are at present not available. It is known, however, that the energy dependence of the moments is asymptotically controlled by $\gamma_{DIS}(\eta^*)$ or $\gamma_{ee}(\eta^*)$ [74]. It is therefore likely that the differences between the C-moments in DIS and e^+e^-, described in Sect. 4.2.3, are a further reflection of suppressed gluon emission in DIS.

Finally, the comparison between $\langle n \rangle$ and $\langle E_T \rangle$ in Fig. 8 demonstrates that both evolve

[12] For further discussion and references see [57], Chapt. 4.

with energy rather similarly. This suggests that the increase of mean transverse energy with increasing W (decreasing x_B) at fixed Q^2, previously observed in this experiment [85], follows mainly from an increase of the hadron multiplicity and less so from a rise of the mean transverse momentum of individual hadrons. A direct measurement of the energy dependence of the transverse momentum distribution in or near the central region of deep-inelastic ep collisions at HERA, and comparison with existing hadron-hadron data, should help to clarify this interesting and theoretically much-debated issue.

5 Summary

Data, fully corrected for detector effects, are presented on the evolution with W and Q^2 of the charged particle multiplicity distribution and its statistical moments, over the ranges $80 < W < 220$ GeV and $10 < Q^2 < 1000$ GeV^2 in subdomains of pseudorapidity space, including the full current hemisphere. The main results can be summarised as follows:

- The mean charged hadron multiplicity and the dispersion, measured in fixed intervals of W and in the domain $1 < \eta^* < 5$ show, within errors, no dependence on the virtuality of the exchanged boson over the Q^2-range covered by H1.

- The low-order moments of the multiplicity distribution in the full current hemisphere show noteworthy similarities with single-hemisphere data in e^+e^- annihilation, in conformity with the hypothesis of approximate environmental independence of quark hadronisation. In particular, the mean charged hadron multiplicity in DIS shows a similar rate of increase with W to that measured in e^+e^- annihilation up to 130 GeV. Analytical predictions from perturbative QCD on the mean parton multiplicity in jets, which are proven to be valid for hadrons in e^+e^- annihilation, are therefore confirmed for the first time in DIS at higher energies than presently reachable at LEP. Data on the second-order factorial moment show that higher-order QCD corrections and/or non-perturbative effects remain significant at present energies.

- The analysis of the multiplicity distribution in pseudorapidity domains of varying size proves that the well-documented property of KNO-scaling, a general characteristic of scale-invariant stochastic branching processes, remains valid in DIS at HERA for small and for large pseudorapidity intervals, but not in intermediate-size domains. The KNO-phenomenon, also predicted in QCD at asymptotic energies, results from an intricate interplay of correlations, different in different types of collisions, and changing rapidly over phase space. The KNO-function in the region $1 < \eta^* < 5$ is strikingly similar to that expected for e^+e^- annihilation under the same kinematical conditions.

- The charged particle density near the central region of the γ^*p centre-of-mass system grows significantly more slowly in DIS than in e^+e^-annihilation. The strength of particle correlations, as reflected in the C-moments, is much larger in the latter process for small pseudorapidity domains. Such differences can be understood within perturbative QCD from calculations of the local anomalous multiplicity dimensions within the Lund dipole formalism. The comparison between e^+e^- annihilation and DIS data provides direct evidence for the "antenna-suppression" effect in current fragmentation, a characteristic of deep-inelastic lepton-hadron dynamics at small Bjorken-x. The same mechanism offers a qualitative explanation for the absence of a multi-jet induced shoulder structure in the DIS multiplicity distributions in intermediate-size pseudorapidity domains, now well established in e^+e^- annihilation data at LEP.

- The charged particle density near the central plateau in the deep-inelastic process is of the same magnitude as that for minimum-bias non-single-diffractive hadron-hadron interactions at the same value of the centre-of-mass energy. Its evolution with W is also comparable to that in hadron-hadron collisions measured up to 900 GeV. However, hadron-hadron collisions are characterised by substantially stronger correlations in small pseudorapidity domains. These features remain to be understood within the Gribov-Feynman pictures of DIS.

- A comparison of the evolution with W of mean transverse energy flow and charged particle density near the central region in DIS shows that the two phenomena are strongly correlated. The striking similarity with the behaviour seen in non-single-diffractive hadron-hadron collisions implies that a theoretical explanation within QCD should simultaneously address the dynamics of both types of process.

- The multiplicity distributions in the smallest η^* domain examined can be well parameterised with Lognormal or Negative Binomial functions. However, the quality of the fits deteriorates in larger domains. The large-n tail of the experimental distributions is well described but deviations occur for small multiplicities. Nevertheless, as economic representations of the data, these parametric forms continue to be useful for phenomenology.

- Among a variety of Monte Carlo generators presently being developed for DIS, we have shown predictions from MEPS 6.4. This model overestimates the mean charged multiplicity in the full current hemisphere, as well as in subdomains of pseudorapidity space. Higher-order moments of the multiplicity distributions are reasonably well described.

Acknowledgements
We are very grateful to the HERA machine group whose outstanding efforts made this experiment possible. We acknowledge the support of the DESY technical staff. We appreciate the big effort of the engineers and technicians who constructed and maintain the detector. We thank the funding agencies for financial support of this experiment. We wish to thank the DESY directorate for the support and hospitality extended to the non-DESY members of the collaboration. Finally, we thank I. Dremin, G. Gustafson, V. Khoze and W. Ochs for stimulating discussions.

References

[1] *Multiparticle Dynamics* (Festschrift L. Van Hove), Eds. A. Giovannini and W.Kittel (World Scientific, Singapore 1990);
G. Giacomelli, Int. J. Mod. Phys. **A5** (1990) 223.

[2] For comprehensive reviews see N. Schmitz, Int. J. Mod. Phys. **A3** (1988) 1997; *ibid.* **A8** (1993) 1993.

[3] P. Carruthers, C.C. Shih, Int. J. Mod. Phys. **A2** (1987) 1447.

[4] I.M. Dremin, *Quantum Chromodynamics and Multiplicity Distributions*, Physics-Uspekhi **37** (1994) 4077.

[5] R. Ugoccioni, A. Giovannini, S. Lupia, *Multiplicity Distributions* in Proc. XXIV Int. Symp. on Multiparticle Dynamics, Vietri-sul-Mare, Italy, 1994, Eds. A. Giovannini, S. Lupia, R.Ugoccioni (World Scientific, Singapore 1995) p.384.

[6] W. Heisenberg, Z.Phys. **113** (1939) 61; Nature (London) **164** (1949) 65;
E. Fermi, Prog. Theor. Phys. **5** (1950) 570.

[7] A. Białas, F. Hayot, Phys. Rev. **D33** (1986) 39.

[8] E.A. De Wolf, I.M. Dremin, W. Kittel, Phys. Rep. **C 270** (1996) 1.

[9] ZEUS Collaboration, M. Derrick *et al.*, Z. Physik **C67** (1995) 93.

[10] H1 Collaboration, S. Aid *et al.*, Nucl. Phys. **B445** (1995) 3;
H1 Collaboration, *Evolution of fragmentation functions and multiplicity distributions in ep DIS in the Breit frame of reference*, paper pa02-072 submitted to 28th Int. Conf. on High Energy Physics ICHEP'96, Warsaw, Poland, 1996.

[11] A.H. Mueller, Phys. Rev. **D4** (1971) 150.

[12] Z.Koba, H.B. Nielsen and P. Olesen, Nucl. Phys. **B40** (1972) 317.

[13] R.P. Feynman, Phys. Rev. Lett. **23** (1969) 1415.

[14] A.I. Golokhvastov, Sov. J. of Nucl. Phys. **27** (1978) 430; *ibid.* **30** (1979) 128.

[15] For a review see W. Ochs, *Scaling and Scale breaking phenomena in multiparticle production*, in Proc. XX Int. Symp. on Multiparticle Dynamics, Gut Holmecke, Germany, 1990, Eds. R. Baier and D. Wegener (World Scientific, Singapore 1991) p. 434.

[16] S. Carius, G. Ingelman, Phys. Lett. **B252** (1990) 647;
G. Wrochna, *How to fit the Lognormal*, preprint Univ. of Warsaw, IFD/8/1990 (1990);
R. Szwed, G. Wrochna and A.K. Wroblewski, Mod. Phys. Lett. **A6** (1991) 245;
M.Gazdzicki *et al.*, Mod. Phys. Lett. **A6** (1991) 981.

[17] R. Szwed, G. Wrochna, Z. Physik **C29** (1985) 255.

[18] UA5 Collaboration, G.J. Alner *et al.*, Phys. Rep. **154** (1987) 247.

[19] UA5 Collaboration, R.E. Ansorge *et al.*, Z. Physik **C43** (1989) 357.

[20] A.M. Polyakov Sov. Phys.–JETP **32** (1971) 296; **33** (1971) 850;
S.J. Orfanidis, V. Rittenberg, Phys. Rev. **D10** (1974) 2892;
G. Cohen-Tannoudji, W. Ochs, Z. Physik **C39** (1988) 513;
W. Ochs, Z. Physik **C23** (1984) 131.

[21] L. Van Hove, A. Giovannini, Acta. Phys. Pol. **B19** (1988) 917;
A. Giovannini, L. Van Hove, Z. Physik **C30** (1986) 391.

[22] A. Giovannini, Nucl. Phys. **B161** (1979) 429.

[23] D. Amati, G. Veneziano, Phys. Lett. **B83** (1979) 87;
G. Marchesini, L. Trentadue, G. Veneziano, Nucl. Phys. **B181** (1981) 335;
Ya.I. Azimov *et al.*, Z. Physik **C27** (1985) 65; *ibid.* **31** (1986) 213.

[24] E.D. Malaza, B.R. Webber, Nucl. Phys. **B267** (1986) 702;
E.D. Malaza, B.R. Webber, Phys. Lett. **B149** (1984) 510.

[25] G. Gustafson, Nucl. Phys. **B392** (1993) 251;
G. Gustafson, M. Olsson, Nucl. Phys. **B406** (1993) 293.

[26] Yu.L. Dokshitzer, Phys. Lett. **B305** (1993) 295.

[27] DELPHI Collaboration, P. Abreu *et al.*, Z. Physik **C50** (1991) 185; *ibid.* **C52** (1991) 271; *ibid.* **C56** (1992) 63.

[28] ALEPH Collaboration, D. Buskulic *et al.*, Z. Physik **C69** (1995) 1.

[29] E665 Collaboration, M.R. Adams *et al.*, Z. Physik **C61** (1994) 179.

[30] A.K. Wróblewski, Acta Phys. Pol. **B4** (1973) 857;
A.J. Buras *et al.*, Phys. Lett. **B47** (1973) 251.

[31] OPAL Collaboration, P.D. Acton *et al.* Z. Physik **C53** (1992) 539.

[32] ALEPH Collaboration, P. Decamp *et al.*, Phys. Lett. **B273** (1991) 181.

[33] WA21 Collaboration, C.T. Jones *et al.*, Z. Physik **C54** (1992) 45.

[34] H1 Collaboration, I. Abt *et al.*, *The H1 detector at HERA*, DESY 93-103 (1993).

[35] H1 Calorimeter Group, B. Andrieu *et al.*, Nucl. Instr. and Meth. **A336** (1993) 460.

[36] H1 Collaboration, T. Ahmed *et al.*, Nucl. Phys. **B249** (1994) 477.

[37] K. Charchula, G. Schuler, H. Spiesberger, CERN-TH.7133/94.

[38] A. Kwiatkowski, H. Spiesberger, H.-J. Möhring, Comp. Phys. Comm. **69** (1992) 155.

[39] G. Ingelman, Proceedings of the 1991 Workshop on Physics at HERA, DESY Vol.3 (1992) 1366.

[40] M. Glück, E. Reya, A. Vogt, Z. Physik **C67** (1995) 433.

[41] L. Lönnblad, Comp. Phys. Comm. **71** (1992) 15.

[42] T. Sjöstrand, Comp. Phys. Comm. **39** (1986) 346;
T. Sjöstrand, M. Bengtsson, ibid. 43 (1987) 367.

[43] B. Andersson *et al.*, Phys. Rep. **97** (1983) 31.

[44] G. Marchesini *et al.*, Comp. Phys. Comm. **67** (1992) 465.

[45] R. Brun *et al.*, GEANT3, CERN DD/EE/84-1 (1987).

[46] TASSO Collaboration, W. Braunschweig *et al.*, Z. Physik **C45** (1989) 193.

[47] AMY Collaboration, H.W. Zheng *et al.*, Phys. Rev. **D42** (1990) 737.

[48] DELPHI Collaboration, P. Abreu *et al.*, Z. Physik **C52** (1991) 271; Z. Physik **C56** (1992) 63.

[49] H1 Collaboration, S. Aid *et al.*, Nucl. Phys. **B470** (1996) 3.

[50] ZEUS Collaboration, M. Derrick *et al.*, Z. Physik **C68** (1995) 29;
H1 Collaboration, S. Aid *et al.*, *Strangeness Production in Deep Inelastic Positron Proton Scattering at HERA*, DESY 96-122; hep-ex/9607010.

[51] HRS Collaboration, M. Derrick *et al.*, Phys. Rev. **D34** (1986) 3304.

[52] DELPHI Collaboration, P. Abreu *et al.*, *Tuning and test of fragmentation models based on identified particles and precision event shape data*, contributed paper eps0548 to EPS-HEP95, Brussels 1995.

[53] DELPHI Collaboration, P. Abreu *et al.*, Phys. Lett. **B372** (1996) 172.

[54] A. De Angelis in Proc. Int. Europhysics Conf. on High Energy Physics, Brussels 1995, Eds. J. Lemonne, C. Vander Velde, F. Verbeure (World Scientific Singapore, 1996) p. 63.

[55] WA25 Collaboration, B. Jongejans *et al.*, Nuovo Cim. **A101** (1989) 435.

[56] European Muon Collaboration, M. Arneodo *et al.*, Z. Physik **C35** (1987) 335.

[57] Yu.L. Dokshitzer *et al.*, *Basics of Perturbative QCD* (Editions Frontières, Gif-sur-Yvette, 1991).

[58] S. Lupia, W. Ochs, Phys. Lett. **B365** (1996) 334.

[59] B.R. Webber, Phys. Lett. **143B** (1984) 501 and refs. therein.

[60] M. Virchaux, A. Milszstajn, Phys. Lett. **B274** (1992) 221.

[61] EMC Collaboration, M. Arneodo *et al.*, Nucl. Phys. **B258** (1985) 249.

[62] W. Ochs, *QCD predictions on multiparticle final states*, in Proc. XXIV Int. Symp. on Multiparticle Dynamics, Vietri-sul-Mare, Italy, 1994, Eds. A. Giovannini, S. Lupia, R.Ugoccioni (World Scientific, Singapore 1995) p. 243.

[63] D. Kant, University of London thesis, also published by the Rutherford Appleton Laboratory as RAL-TH-96-008.

[64] EMC Collaboration, M. Arneodo *et al.*, Z. Physik **C35** (1987) 417.

[65] E665 Collaboration, M.R. Adams *et al.*, Phys. Lett. **B272** (1991) 163.

[66] H1 Collaboration, I. Abt *et al.*, Z. Physik **C63** (1994) 377.

[67] ZEUS Collaboration, M. Derrick *et al.*, Z. Physik **C70** (1996) 1.

[68] OPAL Collaboration, P.D. Acton *et al.*, Phys. Lett. **B287** (1993) 401.

[69] P.H. Garbincius *et al.*, Phys. Rev. Lett. **32** (1974) 328;
A.J. Sadoff *et al.*, Phys. Rev. Lett. **32** (1974) 955;
J. Ballam *et al.*, Phys. Lett. **56B** (1975) 193;
B. Gibbard *et al.*, Phys. Rev. **D11** (1975) 2367;
C. del Papa *et al.*, Phys. Rev. **D13** (1976) 2934;
C.K. Chen *et al.*, Nucl. Phys. **B133** (1978) 13;
M. Derrick *et al.*, Phys. Lett. **91B** (1980) 470;
P. Allen *et al.*, Nucl. Phys. **B181** (1981) 385;
EMC Collaboration, J.J. Aubert *et al.*, Phys. Lett. **114B** (1982) 373;
V.V. Amossov *et al.*, Nucl. Phys. **B203** (1982) 1;
B. Barlag *et al.*, Z. Physik **C11** (1982) 283, **C14** (1982) 281, erratum;
H. Grässler *et al.*, Nucl. Phys. **B233** (1983) 269;
EMC Collaboration, M. Arneodo *et al.*, Phys. Lett. **165B** (1985) 222.

[70] J.D. Bjorken, J. Kogut, Phys. Rev. **D8** (1973) 1341.

[71] R.N. Cahn, J.W. Cleymans, E.W. Colglazier,Phys. Lett. **34B** (1973) 323.

[72] EMC Collaboration, M. Arneodo *et al.*, Z. Physik **C31** (1986) 1; Phys. Lett. **B165** (1985) 222.

[73] WA21 Collaboration, C.T. Jones *et al.*, Z. Physik **C51** (1991) 11.

[74] P. Dahlqvist, G. Gustafson, B. Andersson, Nucl. Phys. **B328** (1989) 76;
G. Gustafson, A. Nilsson, Nucl. Phys. **B355** (1991) 106;
G. Gustafson, C. Sjögren, Phys. Lett. **B248** (1990) 430.

[75] B. Andersson *et al.*, Z. Physik **C49** (1991) 79.

[76] M. Plümer, R.M. Weiner, Phys. Rev. **D37** (1988) 3136.

[77] NA22 Collaboration, M. Adamus *et al.*, Z. Physik **C37** (1988) 215.

[78] A. De Roeck, Ph.D. thesis, Univ. of Antwerpen, 1988 (unpublished).

[79] A. Breakstone *et al.*, Nuovo Cim. **A102** (1989) 1199.

[80] UA1 Collaboration, C. Albajar *et al.*, Nucl. Phys. **B335** (1990) 261.

[81] H1 Collaboration, S. Aid *et al.*, Phys. Lett. **B358** (1995) 412.

[82] H.U. Bengtsson, T. Sjöstrand, Comp. Phys. Com. **46** (1987) 43.

[83] A. Capella, J. Tran Thanh Van, Z. Physik **C23** (1984) 165.

[84] B.Andersson, G.Gustafson, B.Nilsson-Almqvist, Nucl. Phys. **B281** (1987) 289.

[85] H1 Collaboration, S. Aid *et al.*, Phys. Lett. **B356** (1995) 118.

W range (GeV)	$\langle W \rangle$ (GeV)	Q^2 range (GeV^2)	$\langle Q^2 \rangle$ (GeV^2)	♯ events
80 → 115	96.9	10 → 20	13.9	9150
		20 → 40	27.6	5021
		40 → 80	55.0	2509
		200 → 1000	385.3	377
		10 → 80	22.9	16680
115 → 150	132.0	10 → 20	13.9	8202
		20 → 40	27.5	4360
		40 → 80	55.1	2421
		200 → 1000	372.8	411
		10 → 80	23.2	14983
150 → 185	166.8	10 → 20	13.9	6778
		20 → 40	27.6	3662
		40 → 80	55.1	1751
		200 → 1000	378.4	439
		10 → 80	23.3	12191
185 → 220	201.9	10 → 20	13.9	5299
		20 → 40	27.6	2919
		40 → 80	54.9	1037
		200 → 1000	374.2	349
		10 → 80	23.5	9255

Table 1: Number of events, mean Q^2 and mean W in the different kinematical regions studied.

	$\eta^* > 0$				$1 < \eta^* < 3$			
W (GeV)	$80 \div 115$	$115 \div 150$	$150 \div 185$	$185 \div 220$	$80 \div 115$	$115 \div 150$	$150 \div 185$	$185 \div 220$
photo-production	−0.7% (1.3%)	−0.8% (1.5%)	−0.8% (1.6%)	−0.0% (2.2%)	−0.9% (1.7%)	−1.2% (2.4%)	−0.5% (2.5%)	+0.3% (3.3%)
BEMC energy scale	−2.1% (1.2%)	−1.7% (1.5%)	−0.8% (1.5%)	+0.2% (1.7%)	−0.4% (1.4%)	−1.1% (2.0%)	+2.7% (2.2%)	+2.4% (2.8%)
track selection	−4.0% (1.2%)	−3.7% (1.5%)	−3.9% (1.6%)	−3.1% (1.5%)	−3.0% (2.1%)	−3.5% (1.9%)	−4.3% (2.0%)	−4.5% (2.4%)
unfolding method	+0.1% (1.2%)	−0.8% (1.4%)	+0.9% (1.7%)	+1.8% (1.8%)	+0.6% (1.7%)	−1.2% (1.9%)	+1.4% (2.4%)	+1.1% (2.7%)
LEPTO 6.1	−4.9% (1.6%)	−4.5% (0.9%)	−4.6% (1.2%)	−3.8% (1.2%)	−0.7% (1.1%)	−2.3% (1.0%)	−2.5% (1.2%)	−2.1% (1.2%)
TOTAL	6.8%	6.6%	6.6%	5.9%	3.7%	5.3%	6.4%	6.5%

Table 2: Summary of systematic effects. The change in average multiplicity is given for the full current hemisphere and for a restricted pseudorapidity interval. For comparison, the statistical error on $\langle n \rangle$ for the given data sample is given in brackets.

80 GeV $< W <$ 115 GeV

n	P_n (%) $1 < \eta^* < 2$	$1 < \eta^* < 3$	$1 < \eta^* < 4$	$1 < \eta^* < 5$
0	15.79 ± 0.52 ± 2.18	3.26 ± 0.22 ± 1.58	0.78 ± 0.09 ± 1.66	0.40† ± 0.08
1	22.55 ± 0.50 ± 1.92	8.01 ± 0.27 ± 1.29	2.73 ± 0.18 ± 0.94	1.64 ± 0.16 ± 0.39
2	20.62 ± 0.46 ± 1.24	12.84 ± 0.35 ± 1.30	5.73 ± 0.28 ± 1.45	3.82 ± 0.22 ± 1.27
3	15.96 ± 0.43 ± 2.29	14.03 ± 0.35 ± 1.21	9.55 ± 0.29 ± 1.46	7.59 ± 0.28 ± 1.06
4	10.21 ± 0.37 ± 1.06	13.38 ± 0.32 ± 2.22	11.11 ± 0.32 ± 1.21	10.08 ± 0.34 ± 1.18
5	6.07 ± 0.30 ± 1.54	11.73 ± 0.35 ± 0.46	12.76 ± 0.35 ± 2.22	12.30 ± 0.34 ± 0.89
6	3.85 ± 0.26 ± 0.48	9.84 ± 0.34 ± 0.71	12.19 ± 0.32 ± 1.28	12.91 ± 0.35 ± 1.29
7	2.24 ± 0.16 ± 0.62	7.94 ± 0.33 ± 0.52	11.17 ± 0.37 ± 0.96	12.27 ± 0.35 ± 1.86
8	1.15 ± 0.12 ± 0.42	5.91 ± 0.32 ± 1.20	9.22 ± 0.31 ± 0.48	10.65 ± 0.33 ± 0.86
9	0.68 ± 0.10 ± 0.31	4.00 ± 0.21 ± 0.82	7.72 ± 0.33 ± 1.37	8.69 ± 0.30 ± 1.08
10	0.49 ± 0.12 ± 0.24	3.21 ± 0.19 ± 0.56	5.69 ± 0.24 ± 1.31	6.38 ± 0.26 ± 0.99
11	0.19 ± 0.06 ± 0.26	2.22 ± 0.18 ± 1.06	3.95 ± 0.22 ± 1.00	4.79 ± 0.25 ± 1.23
12	0.07 ± 0.04 ± 0.13	1.49 ± 0.14 ± 0.66	2.76 ± 0.23 ± 0.96	3.20 ± 0.24 ± 0.97
13	0.05 ± 0.03 ± 0.06	0.90 ± 0.15 ± 0.53	1.79 ± 0.18 ± 0.80	2.05 ± 0.19 ± 0.69
14		0.54 ± 0.11 ± 0.53	1.22 ± 0.15 ± 0.62	1.38 ± 0.16 ± 0.74
15		0.36 ± 0.08 ± 0.57	0.67 ± 0.12 ± 0.68	0.86 ± 0.14 ± 0.66
16		0.14 ± 0.07 ± 0.19	0.40 ± 0.11 ± 0.43	0.40 ± 0.08 ± 0.24
17		0.08 ± 0.05 ± 0.10	0.24 ± 0.11 ± 0.33	0.27 ± 0.13 ± 0.37
18			0.13 ± 0.08 ± 0.19	0.10 ± 0.05 ± 0.11

115 GeV $< W <$ 150 GeV

n	P_n (%) $1 < \eta^* < 2$	$1 < \eta^* < 3$	$1 < \eta^* < 4$	$1 < \eta^* < 5$
0	16.80 ± 0.62 ± 0.55	4.52 ± 0.35 ± 1.19	1.09 ± 0.18 ± 0.77	0.35† ± 0.08
1	21.55 ± 0.54 ± 1.05	8.00 ± 0.35 ± 1.21	2.57 ± 0.19 ± 1.12	1.17 ± 0.13 ± 0.62
2	19.69 ± 0.50 ± 0.53	12.15 ± 0.36 ± 0.70	4.72 ± 0.24 ± 0.70	2.58 ± 0.14 ± 1.26
3	15.19 ± 0.48 ± 0.77	12.96 ± 0.36 ± 0.91	8.09 ± 0.29 ± 0.74	5.63 ± 0.23 ± 0.69
4	10.54 ± 0.36 ± 0.31	12.74 ± 0.38 ± 0.74	9.96 ± 0.33 ± 0.95	7.97 ± 0.24 ± 1.03
5	6.76 ± 0.34 ± 0.75	11.09 ± 0.32 ± 1.63	11.23 ± 0.36 ± 0.95	10.36 ± 0.31 ± 0.82
6	4.17 ± 0.27 ± 0.50	9.35 ± 0.31 ± 0.70	11.27 ± 0.33 ± 1.37	11.44 ± 0.37 ± 0.56
7	2.55 ± 0.20 ± 0.76	7.31 ± 0.27 ± 2.06	10.32 ± 0.31 ± 0.25	11.96 ± 0.35 ± 1.18
8	1.29 ± 0.14 ± 0.48	6.01 ± 0.29 ± 0.93	9.21 ± 0.34 ± 0.52	10.41 ± 0.32 ± 0.66
9	0.64 ± 0.10 ± 0.62	4.53 ± 0.24 ± 1.38	8.03 ± 0.30 ± 0.29	9.65 ± 0.36 ± 0.74
10	0.31 ± 0.07 ± 0.14	3.76 ± 0.25 ± 0.53	6.51 ± 0.29 ± 0.87	7.88 ± 0.28 ± 0.49
11	0.20 ± 0.04 ± 0.07	2.57 ± 0.23 ± 0.86	5.32 ± 0.26 ± 0.88	6.15 ± 0.23 ± 0.80
12	0.12 ± 0.03 ± 0.15	1.90 ± 0.18 ± 0.77	3.84 ± 0.23 ± 0.88	4.96 ± 0.27 ± 1.35
13	0.07 ± 0.03 ± 0.07	1.05 ± 0.16 ± 0.29	2.96 ± 0.23 ± 0.53	3.51 ± 0.25 ± 0.50
14	0.03 ± 0.02 ± 0.04	0.77 ± 0.12 ± 0.54	1.81 ± 0.18 ± 0.65	2.15 ± 0.21 ± 0.45
15		0.56 ± 0.10 ± 0.48	1.25 ± 0.16 ± 0.33	1.47 ± 0.17 ± 0.43
16		0.31 ± 0.08 ± 0.24	0.76 ± 0.12 ± 0.62	0.93 ± 0.14 ± 0.92
17		0.18 ± 0.06 ± 0.28	0.46 ± 0.10 ± 0.29	0.72 ± 0.17 ± 0.62
18		0.12 ± 0.06 ± 0.12	0.25 ± 0.09 ± 0.20	0.25 ± 0.08 ± 0.34
19			0.14 ± 0.06 ± 0.23	0.17 ± 0.07 ± 0.24
20			0.08 ± 0.05 ± 0.11	0.12 ± 0.08 ± 0.13
21				0.03 ± 0.02 ± 0.03

Table 3: The fully corrected multiplicity distribution P_n (%). The first error is the statistical error, the second the systematic uncertainty of the result.

† The value of P_0 in the domain $1 < \eta^* < 5$ is not measured but taken from the reweighted DJANGO 6.0 Monte Carlo generator.

150 GeV $< W <$ 185 GeV

n	P_n (%) $1<\eta^*<2$	$1<\eta^*<3$	$1<\eta^*<4$	$1<\eta^*<5$
0	16.01 ± 0.58 ± 5.43	4.24 ± 0.36 ± 3.19	1.13 ± 0.15 ± 1.51	$0.28^{\dagger}$ ± 0.08
1	19.56 ± 0.63 ± 1.10	8.32 ± 0.41 ± 1.39	2.56 ± 0.20 ± 1.55	1.09 ± 0.13 ± 1.03
2	19.73 ± 0.54 ± 1.58	10.99 ± 0.40 ± 0.67	4.69 ± 0.24 ± 2.38	2.21 ± 0.14 ± 0.71
3	16.01 ± 0.60 ± 1.37	11.75 ± 0.37 ± 1.30	6.81 ± 0.30 ± 1.00	4.18 ± 0.20 ± 1.28
4	11.19 ± 0.50 ± 1.20	11.71 ± 0.41 ± 1.27	8.77 ± 0.35 ± 1.02	6.61 ± 0.23 ± 2.08
5	7.21 ± 0.34 ± 0.70	11.37 ± 0.41 ± 1.49	9.87 ± 0.38 ± 1.56	8.24 ± 0.31 ± 1.36
6	4.11 ± 0.30 ± 0.81	9.39 ± 0.39 ± 1.08	10.47 ± 0.34 ± 0.32	9.77 ± 0.34 ± 1.20
7	2.80 ± 0.25 ± 0.93	7.98 ± 0.35 ± 0.57	9.68 ± 0.33 ± 0.94	11.04 ± 0.33 ± 0.89
8	1.40 ± 0.17 ± 0.81	6.27 ± 0.38 ± 0.52	9.10 ± 0.34 ± 0.57	10.87 ± 0.34 ± 0.66
9	0.91 ± 0.15 ± 0.48	5.36 ± 0.35 ± 1.07	8.10 ± 0.34 ± 1.05	9.89 ± 0.35 ± 1.13
10	0.33 ± 0.08 ± 0.23	3.64 ± 0.25 ± 1.03	6.90 ± 0.31 ± 0.81	8.18 ± 0.35 ± 0.44
11	0.31 ± 0.07 ± 0.18	2.87 ± 0.22 ± 0.28	5.76 ± 0.30 ± 0.72	7.07 ± 0.31 ± 0.56
12	0.10 ± 0.04 ± 0.10	1.82 ± 0.20 ± 0.73	4.92 ± 0.28 ± 1.17	5.76 ± 0.34 ± 1.15
13	0.13 ± 0.07 ± 0.18	1.24 ± 0.15 ± 0.54	3.59 ± 0.25 ± 1.32	4.88 ± 0.31 ± 1.50
14	0.08 ± 0.06 ± 0.14	1.08 ± 0.16 ± 0.89	2.71 ± 0.24 ± 0.97	3.42 ± 0.26 ± 0.89
15		0.78 ± 0.15 ± 0.61	1.59 ± 0.16 ± 0.72	2.43 ± 0.25 ± 1.00
16		0.43 ± 0.09 ± 0.40	1.11 ± 0.12 ± 0.93	1.31 ± 0.17 ± 0.78
17		0.20 ± 0.06 ± 0.13	0.86 ± 0.13 ± 0.46	1.07 ± 0.19 ± 0.64
18		0.18 ± 0.07 ± 0.13	0.49 ± 0.13 ± 0.32	0.55 ± 0.14 ± 0.51
19		0.13 ± 0.07 ± 0.24	0.31 ± 0.11 ± 0.63	0.43 ± 0.13 ± 0.50
20		0.06 ± 0.05 ± 0.10	0.09 ± 0.05 ± 0.14	0.12 ± 0.05 ± 0.51
21			0.17 ± 0.09 ± 0.30	0.18 ± 0.08 ± 0.32
22			0.13 ± 0.09 ± 0.26	0.16 ± 0.11 ± 0.31

185 GeV $< W <$ 220 GeV

n	P_n (%) $1<\eta^*<2$	$1<\eta^*<3$	$1<\eta^*<4$	$1<\eta^*<5$
0	15.76 ± 0.68 ± 3.11	4.24 ± 0.42 ± 3.18	1.07 ± 0.24 ± 2.96	$0.27^{\dagger}$ ± 0.09
1	19.66 ± 0.76 ± 0.78	8.00 ± 0.45 ± 0.48	2.81 ± 0.30 ± 1.27	0.96 ± 0.13 ± 1.96
2	19.56 ± 0.62 ± 1.75	10.74 ± 0.57 ± 1.52	5.22 ± 0.32 ± 0.73	2.37 ± 0.23 ± 0.68
3	15.76 ± 0.61 ± 2.03	11.51 ± 0.47 ± 0.69	6.70 ± 0.33 ± 0.50	3.73 ± 0.24 ± 1.12
4	11.08 ± 0.58 ± 1.85	11.76 ± 0.48 ± 2.08	7.98 ± 0.37 ± 0.87	5.47 ± 0.27 ± 0.99
5	6.95 ± 0.45 ± 0.86	11.65 ± 0.53 ± 1.27	9.18 ± 0.34 ± 0.58	7.50 ± 0.30 ± 0.83
6	4.63 ± 0.38 ± 0.97	9.74 ± 0.47 ± 1.62	9.07 ± 0.40 ± 0.87	8.49 ± 0.35 ± 1.24
7	3.20 ± 0.32 ± 1.14	7.96 ± 0.43 ± 0.91	10.18 ± 0.50 ± 0.63	10.08 ± 0.39 ± 1.61
8	1.36 ± 0.16 ± 0.74	6.83 ± 0.44 ± 1.06	9.10 ± 0.41 ± 0.68	10.54 ± 0.46 ± 1.18
9	0.95 ± 0.15 ± 0.79	5.12 ± 0.34 ± 1.16	7.95 ± 0.34 ± 1.57	10.40 ± 0.43 ± 1.71
10	0.47 ± 0.12 ± 0.31	3.70 ± 0.30 ± 1.24	7.50 ± 0.34 ± 1.83	9.20 ± 0.44 ± 1.00
11	0.33 ± 0.10 ± 0.50	2.52 ± 0.24 ± 0.88	6.10 ± 0.38 ± 0.78	8.03 ± 0.40 ± 1.12
12	0.11 ± 0.04 ± 0.09	1.79 ± 0.19 ± 0.76	4.98 ± 0.33 ± 1.30	6.48 ± 0.30 ± 0.99
13	0.05 ± 0.04 ± 0.10	1.39 ± 0.17 ± 0.92	3.46 ± 0.26 ± 0.77	4.78 ± 0.29 ± 0.95
14	0.03 ± 0.02 ± 0.05	1.11 ± 0.16 ± 1.23	2.60 ± 0.22 ± 0.75	3.81 ± 0.27 ± 1.22
15		0.66 ± 0.13 ± 0.33	2.03 ± 0.21 ± 0.58	2.32 ± 0.21 ± 0.78
16		0.44 ± 0.10 ± 0.27	1.29 ± 0.16 ± 0.80	2.13 ± 0.22 ± 1.08
17		0.29 ± 0.10 ± 0.19	1.00 ± 0.16 ± 0.65	1.14 ± 0.14 ± 0.67
18		0.14 ± 0.06 ± 0.19	0.71 ± 0.15 ± 0.22	0.83 ± 0.12 ± 0.44
19		0.10 ± 0.05 ± 0.14	0.39 ± 0.09 ± 0.35	0.64 ± 0.14 ± 0.29
20		0.06 ± 0.04 ± 0.29	0.21 ± 0.07 ± 0.18	0.30 ± 0.07 ± 0.39
21		0.05 ± 0.04 ± 0.10	0.17 ± 0.10 ± 0.26	0.13 ± 0.07 ± 0.18
22			0.11 ± 0.04 ± 0.13	0.19 ± 0.08 ± 0.26
23				0.03 ± 0.02 ± 0.05

Table 3: continued

$\eta^* > 0$

W (GeV)	$80 \div 115$	$115 \div 150$	$150 \div 185$	$185 \div 220$
$\langle n_{ch} \rangle$	8.98 $\pm$ 0.07 $\pm$ 0.61	10.00 $\pm$ 0.07 $\pm$ 0.66	10.88 $\pm$ 0.09 $\pm$ 0.72	11.35 $\pm$ 0.09 $\pm$ 0.67
D_2	3.89 $\pm$ 0.07 $\pm$ 0.23	4.16 $\pm$ 0.06 $\pm$ 0.26	4.49 $\pm$ 0.08 $\pm$ 0.36	4.56 $\pm$ 0.08 $\pm$ 0.30
D_3	3.43 $\pm$ 0.16 $\pm$ 0.22	3.41 $\pm$ 0.15 $\pm$ 0.21	3.61 $\pm$ 0.26 $\pm$ 0.55	3.67 $\pm$ 0.25 $\pm$ 0.45
D_4	5.39 $\pm$ 0.15 $\pm$ 0.38	5.58 $\pm$ 0.13 $\pm$ 0.23	6.05 $\pm$ 0.21 $\pm$ 0.71	6.26 $\pm$ 0.19 $\pm$ 0.49
C_2	1.18 $\pm$ 0.00 $\pm$ 0.04	1.17 $\pm$ 0.00 $\pm$ 0.01	1.17 $\pm$ 0.00 $\pm$ 0.02	1.16 $\pm$ 0.00 $\pm$ 0.02
C_3	1.62 $\pm$ 0.02 $\pm$ 0.14	1.56 $\pm$ 0.01 $\pm$ 0.06	1.54 $\pm$ 0.02 $\pm$ 0.08	1.51 $\pm$ 0.02 $\pm$ 0.07
C_4	2.48 $\pm$ 0.07 $\pm$ 0.40	2.29 $\pm$ 0.05 $\pm$ 0.17	2.26 $\pm$ 0.07 $\pm$ 0.21	2.19 $\pm$ 0.06 $\pm$ 0.19
R_2	1.07 $\pm$ 0.00 $\pm$ 0.03	1.07 $\pm$ 0.00 $\pm$ 0.01	1.07 $\pm$ 0.00 $\pm$ 0.02	1.07 $\pm$ 0.00 $\pm$ 0.02
R_3	1.24 $\pm$ 0.02 $\pm$ 0.10	1.22 $\pm$ 0.01 $\pm$ 0.04	1.24 $\pm$ 0.02 $\pm$ 0.07	1.22 $\pm$ 0.02 $\pm$ 0.06

$1 < \eta^* < 2$

W (GeV)	$80 \div 115$	$115 \div 150$	$150 \div 185$	$185 \div 220$
$\langle n_{ch} \rangle$	2.46 $\pm$ 0.03 $\pm$ 0.10	2.50 $\pm$ 0.03 $\pm$ 0.12	2.63 $\pm$ 0.04 $\pm$ 0.18	2.66 $\pm$ 0.04 $\pm$ 0.18
D_2	2.07 $\pm$ 0.05 $\pm$ 0.08	2.13 $\pm$ 0.03 $\pm$ 0.10	2.22 $\pm$ 0.05 $\pm$ 0.12	2.22 $\pm$ 0.03 $\pm$ 0.14
D_3	2.21 $\pm$ 0.11 $\pm$ 0.10	2.24 $\pm$ 0.05 $\pm$ 0.14	2.39 $\pm$ 0.11 $\pm$ 0.18	2.31 $\pm$ 0.07 $\pm$ 0.12
D_4	3.08 $\pm$ 0.16 $\pm$ 0.15	3.15 $\pm$ 0.07 $\pm$ 0.17	3.39 $\pm$ 0.16 $\pm$ 0.26	3.24 $\pm$ 0.09 $\pm$ 0.12
C_2	1.71 $\pm$ 0.02 $\pm$ 0.02	1.72 $\pm$ 0.02 $\pm$ 0.04	1.71 $\pm$ 0.02 $\pm$ 0.05	1.69 $\pm$ 0.02 $\pm$ 0.03
C_3	3.87 $\pm$ 0.16 $\pm$ 0.18	3.90 $\pm$ 0.11 $\pm$ 0.24	3.89 $\pm$ 0.17 $\pm$ 0.18	3.75 $\pm$ 0.12 $\pm$ 0.20
C_4	10.67 $\pm$ 0.93 $\pm$ 1.23	10.77 $\pm$ 0.60 $\pm$ 1.17	11.03 $\pm$ 1.09 $\pm$ 0.63	10.02 $\pm$ 0.65 $\pm$ 1.22
R_2	1.30 $\pm$ 0.02 $\pm$ 0.03	1.32 $\pm$ 0.01 $\pm$ 0.04	1.33 $\pm$ 0.02 $\pm$ 0.04	1.32 $\pm$ 0.02 $\pm$ 0.03
R_3	2.11 $\pm$ 0.14 $\pm$ 0.15	2.15 $\pm$ 0.08 $\pm$ 0.19	2.22 $\pm$ 0.14 $\pm$ 0.14	2.11 $\pm$ 0.09 $\pm$ 0.13
K_3	0.187 $\pm$ 0.070 $\pm$ 0.097	0.167 $\pm$ 0.040 $\pm$ 0.063	0.226 $\pm$ 0.079 $\pm$ 0.085	0.147 $\pm$ 0.043 $\pm$ 0.101

$1 < \eta^* < 3$

W (GeV)	$80 \div 115$	$115 \div 150$	$150 \div 185$	$185 \div 220$
$\langle n_{ch} \rangle$	4.90 $\pm$ 0.04 $\pm$ 0.18	5.06 $\pm$ 0.05 $\pm$ 0.27	5.32 $\pm$ 0.07 $\pm$ 0.34	5.35 $\pm$ 0.06 $\pm$ 0.35
D_2	3.10 $\pm$ 0.04 $\pm$ 0.13	3.37 $\pm$ 0.04 $\pm$ 0.21	3.57 $\pm$ 0.06 $\pm$ 0.26	3.58 $\pm$ 0.07 $\pm$ 0.30
D_3	2.91 $\pm$ 0.10 $\pm$ 0.25	3.18 $\pm$ 0.09 $\pm$ 0.21	3.45 $\pm$ 0.12 $\pm$ 0.43	3.54 $\pm$ 0.20 $\pm$ 0.34
D_4	4.27 $\pm$ 0.11 $\pm$ 0.28	4.62 $\pm$ 0.10 $\pm$ 0.27	5.01 $\pm$ 0.13 $\pm$ 0.45	5.18 $\pm$ 0.28 $\pm$ 0.45
C_2	1.40 $\pm$ 0.01 $\pm$ 0.03	1.44 $\pm$ 0.01 $\pm$ 0.02	1.45 $\pm$ 0.01 $\pm$ 0.02	1.44 $\pm$ 0.01 $\pm$ 0.02
C_3	2.41 $\pm$ 0.04 $\pm$ 0.16	2.57 $\pm$ 0.05 $\pm$ 0.10	2.62 $\pm$ 0.07 $\pm$ 0.14	2.62 $\pm$ 0.09 $\pm$ 0.09
C_4	4.83 $\pm$ 0.19 $\pm$ 0.64	5.34 $\pm$ 0.20 $\pm$ 0.38	5.57 $\pm$ 0.28 $\pm$ 0.68	5.71 $\pm$ 0.47 $\pm$ 0.34
R_2	1.19 $\pm$ 0.01 $\pm$ 0.03	1.24 $\pm$ 0.01 $\pm$ 0.02	1.26 $\pm$ 0.01 $\pm$ 0.02	1.26 $\pm$ 0.01 $\pm$ 0.03
R_3	1.64 $\pm$ 0.04 $\pm$ 0.13	1.80 $\pm$ 0.04 $\pm$ 0.09	1.87 $\pm$ 0.06 $\pm$ 0.13	1.88 $\pm$ 0.08 $\pm$ 0.11
K_3	0.048 $\pm$ 0.015 $\pm$ 0.044	0.063 $\pm$ 0.016 $\pm$ 0.033	0.088 $\pm$ 0.022 $\pm$ 0.077	0.108 $\pm$ 0.041 $\pm$ 0.036

$1 < \eta^* < 4$

W (GeV)	$80 \div 115$	$115 \div 150$	$150 \div 185$	$185 \div 220$
$\langle n_{ch} \rangle$	6.45 $\pm$ 0.06 $\pm$ 0.33	7.00 $\pm$ 0.05 $\pm$ 0.35	7.51 $\pm$ 0.06 $\pm$ 0.51	7.66 $\pm$ 0.07 $\pm$ 0.47
D_2	3.23 $\pm$ 0.09 $\pm$ 0.14	3.57 $\pm$ 0.04 $\pm$ 0.23	3.93 $\pm$ 0.06 $\pm$ 0.25	4.06 $\pm$ 0.06 $\pm$ 0.20
D_3	2.71 $\pm$ 0.28 $\pm$ 0.21	2.89 $\pm$ 0.11 $\pm$ 0.23	3.28 $\pm$ 0.14 $\pm$ 0.50	3.32 $\pm$ 0.16 $\pm$ 0.28
D_4	4.34 $\pm$ 0.27 $\pm$ 0.24	4.72 $\pm$ 0.10 $\pm$ 0.20	5.29 $\pm$ 0.14 $\pm$ 0.44	5.41 $\pm$ 0.14 $\pm$ 0.22
C_2	1.25 $\pm$ 0.01 $\pm$ 0.03	1.26 $\pm$ 0.00 $\pm$ 0.02	1.27 $\pm$ 0.00 $\pm$ 0.02	1.28 $\pm$ 0.00 $\pm$ 0.02
C_3	1.82 $\pm$ 0.05 $\pm$ 0.13	1.85 $\pm$ 0.02 $\pm$ 0.07	1.90 $\pm$ 0.03 $\pm$ 0.08	1.92 $\pm$ 0.03 $\pm$ 0.08
C_4	3.01 $\pm$ 0.20 $\pm$ 0.38	3.04 $\pm$ 0.08 $\pm$ 0.22	3.22 $\pm$ 0.11 $\pm$ 0.27	3.26 $\pm$ 0.12 $\pm$ 0.26
R_2	1.09 $\pm$ 0.01 $\pm$ 0.03	1.11 $\pm$ 0.00 $\pm$ 0.02	1.14 $\pm$ 0.00 $\pm$ 0.02	1.15 $\pm$ 0.00 $\pm$ 0.02
R_3	1.29 $\pm$ 0.05 $\pm$ 0.09	1.35 $\pm$ 0.02 $\pm$ 0.06	1.43 $\pm$ 0.03 $\pm$ 0.07	1.45 $\pm$ 0.03 $\pm$ 0.06

Table 4: Moments and cumulants of the unfolded multiplicity distribution for different ranges in pseudorapidity η^* and intervals in W.

$1 < \eta^* < 5$

W (GeV)	$80 \div 115$	$115 \div 150$	$150 \div 185$	$185 \div 220$
$\langle n_{ch} \rangle$	6.90 ± 0.05 ± 0.34	7.72 ± 0.05 ± 0.42	8.45 ± 0.06 ± 0.58	8.81 ± 0.08 ± 0.54
D_2	3.15 ± 0.05 ± 0.21	3.45 ± 0.04 ± 0.25	3.77 ± 0.06 ± 0.25	3.86 ± 0.05 ± 0.22
D_3	2.56 ± 0.12 ± 0.33	2.74 ± 0.13 ± 0.19	3.02 ± 0.18 ± 0.54	2.95 ± 0.19 ± 0.41
D_4	4.23 ± 0.11 ± 0.37	4.59 ± 0.10 ± 0.29	5.08 ± 0.15 ± 0.45	5.17 ± 0.14 ± 0.29
C_2	1.20 ± 0.00 ± 0.03	1.19 ± 0.00 ± 0.02	1.19 ± 0.00 ± 0.02	1.19 ± 0.00 ± 0.02
C_3	1.67 ± 0.02 ± 0.12	1.64 ± 0.02 ± 0.06	1.64 ± 0.02 ± 0.08	1.61 ± 0.02 ± 0.08
C_4	2.60 ± 0.07 ± 0.35	2.50 ± 0.06 ± 0.16	2.50 ± 0.08 ± 0.24	2.42 ± 0.07 ± 0.21
R_2	1.06 ± 0.00 ± 0.02	1.07 ± 0.00 ± 0.02	1.08 ± 0.00 ± 0.02	1.07 ± 0.00 ± 0.02
R_3	1.19 ± 0.02 ± 0.09	1.21 ± 0.01 ± 0.05	1.24 ± 0.02 ± 0.07	1.23 ± 0.02 ± 0.06

$2 < \eta^* < 3$

W (GeV)	$80 \div 115$	$115 \div 150$	$150 \div 185$	$185 \div 220$
$\langle n_{ch} \rangle$	2.46 ± 0.03 ± 0.17	2.61 ± 0.03 ± 0.20	2.73 ± 0.04 ± 0.27	2.71 ± 0.04 ± 0.20
D_2	1.92 ± 0.03 ± 0.19	2.11 ± 0.03 ± 0.16	2.24 ± 0.04 ± 0.20	2.22 ± 0.03 ± 0.18
D_3	1.86 ± 0.05 ± 0.10	2.07 ± 0.06 ± 0.14	2.23 ± 0.08 ± 0.13	2.28 ± 0.07 ± 0.22
D_4	2.67 ± 0.06 ± 0.12	2.94 ± 0.08 ± 0.21	3.14 ± 0.09 ± 0.18	3.20 ± 0.09 ± 0.25
C_2	1.61 ± 0.01 ± 0.03	1.65 ± 0.01 ± 0.03	1.67 ± 0.01 ± 0.05	1.67 ± 0.02 ± 0.06
C_3	3.26 ± 0.08 ± 0.16	3.47 ± 0.10 ± 0.15	3.57 ± 0.10 ± 0.25	3.60 ± 0.11 ± 0.30
C_4	7.77 ± 0.35 ± 0.79	8.57 ± 0.48 ± 0.60	8.99 ± 0.52 ± 1.20	9.30 ± 0.56 ± 1.19
R_2	1.20 ± 0.01 ± 0.02	1.27 ± 0.01 ± 0.04	1.30 ± 0.01 ± 0.05	1.30 ± 0.02 ± 0.06
R_3	1.63 ± 0.05 ± 0.10	1.86 ± 0.08 ± 0.13	1.99 ± 0.08 ± 0.14	2.02 ± 0.09 ± 0.25
K_3	0.018 ± 0.021 ± 0.041	0.043 ± 0.030 ± 0.035	0.072 ± 0.040 ± 0.062	0.121 ± 0.038 ± 0.076

$3 < \eta^* < 4$

W (GeV)	$80 \div 115$	$115 \div 150$	$150 \div 185$	$185 \div 220$
$\langle n_{ch} \rangle$	1.54 ± 0.02 ± 0.18	1.93 ± 0.02 ± 0.17	2.17 ± 0.02 ± 0.18	2.29 ± 0.03 ± 0.17
D_2	1.32 ± 0.01 ± 0.14	1.48 ± 0.02 ± 0.14	1.59 ± 0.02 ± 0.09	1.67 ± 0.03 ± 0.10
D_3	1.23 ± 0.03 ± 0.07	1.33 ± 0.03 ± 0.09	1.39 ± 0.05 ± 0.04	1.54 ± 0.05 ± 0.16
D_4	1.79 ± 0.03 ± 0.11	2.01 ± 0.04 ± 0.10	2.14 ± 0.06 ± 0.06	2.31 ± 0.06 ± 0.17
C_2	1.73 ± 0.01 ± 0.11	1.58 ± 0.01 ± 0.10	1.53 ± 0.01 ± 0.06	1.53 ± 0.01 ± 0.10
C_3	3.70 ± 0.08 ± 0.55	3.08 ± 0.07 ± 0.47	2.87 ± 0.07 ± 0.26	2.91 ± 0.08 ± 0.46
C_4	9.24 ± 0.38 ± 2.29	6.99 ± 0.28 ± 1.72	6.21 ± 0.31 ± 1.00	6.47 ± 0.34 ± 1.70
R_2	1.08 ± 0.01 ± 0.04	1.07 ± 0.01 ± 0.07	1.07 ± 0.01 ± 0.03	1.09 ± 0.01 ± 0.08
R_3	1.17 ± 0.05 ± 0.15	1.16 ± 0.04 ± 0.19	1.18 ± 0.05 ± 0.08	1.28 ± 0.05 ± 0.24
K_3	0.079 ± 0.019 ± 0.062	0.045 ± 0.014 ± 0.040	0.054 ± 0.018 ± 0.033	0.011 ± 0.017 ± 0.068

$4 < \eta^* < 5$

W (GeV)	$80 \div 115$	$115 \div 150$	$150 \div 185$	$185 \div 220$
$\langle n_{ch} \rangle$	0.46 ± 0.01 ± 0.04	0.71 ± 0.01 ± 0.04	0.93 ± 0.01 ± 0.09	1.17 ± 0.01 ± 0.09
D_2	0.71 ± 0.01 ± 0.02	0.88 ± 0.01 ± 0.08	0.99 ± 0.01 ± 0.06	1.09 ± 0.01 ± 0.19
D_3	0.83 ± 0.02 ± 0.02	0.93 ± 0.01 ± 0.03	0.98 ± 0.02 ± 0.05	1.01 ± 0.02 ± 0.01
D_4	1.09 ± 0.03 ± 0.04	1.26 ± 0.02 ± 0.03	1.37 ± 0.03 ± 0.07	1.47 ± 0.02 ± 0.03
C_2	3.34 ± 0.06 ± 0.11	2.52 ± 0.04 ± 0.18	2.13 ± 0.02 ± 0.09	1.86 ± 0.01 ± 0.11
C_3	13.78 ± 0.61 ± 1.06	7.85 ± 0.30 ± 1.18	5.58 ± 0.17 ± 0.59	4.23 ± 0.10 ± 0.55
C_4	68.80 ± 5.70 ± 9.55	28.93 ± 1.85 ± 6.83	17.21 ± 0.87 ± 3.47	11.24 ± 0.46 ± 2.25
R_2	1.19 ± 0.04 ± 0.06	1.12 ± 0.03 ± 0.10	1.05 ± 0.02 ± 0.05	1.01 ± 0.01 ± 0.05
R_3	1.41 ± 0.24 ± 0.29	1.16 ± 0.09 ± 0.23	1.02 ± 0.07 ± 0.19	0.92 ± 0.04 ± 0.09
K_3	0.159 ± 0.144 ± 0.138	0.221 ± 0.041 ± 0.136	0.150 ± 0.028 ± 0.104	0.109 ± 0.017 ± 0.061

Table 4: continued

$1 < \eta^* < 2$

W (GeV)	$80 \div 115$	$115 \div 150$	$150 \div 185$	$185 \div 220$
$\overline{n}$	2.52 ± 0.10	2.58 ± 0.13	2.72 ± 0.15	2.75 ± 0.19
$1/k$	0.285 ± 0.080	0.288 ± 0.056	0.269 ± 0.034	0.270 ± 0.064
χ^2/NDF	$29.4/13$	$23.0/14$	$33.0/15$	$27.1/14$
m	2.44 ± 0.16	2.49 ± 0.16	2.66 ± 0.20	2.67 ± 0.13
d	0.791 ± 0.092	0.812 ± 0.077	0.743 ± 0.094	0.768 ± 0.122
c	2.6 ± 3.4	3.1 ± 1.2	1.9 ± 1.7	2.5 ± 7.5
χ^2/NDF	$21.8/12$	$8.9/13$	$24.9/14$	$19.8/13$

$1 < \eta^* < 3$

W (GeV)	$80 \div 115$	$115 \div 150$	$150 \div 185$	$185 \div 220$
$\overline{n}$	4.85 ± 0.16	5.12 ± 0.26	5.36 ± 0.25	5.41 ± 0.20
$1/k$	0.161 ± 0.039	0.235 ± 0.017	0.256 ± 0.028	0.245 ± 0.034
χ^2/NDF	$121.6/19$	$54.5/19$	$61.5/21$	$44.7/24$
m	4.79 ± 0.24	5.05 ± 0.30	5.25 ± 0.20	5.32 ± 0.17
d	0.634 ± 0.017	0.644 ± 0.080	0.662 ± 0.074	0.641 ± 0.060
c	4.5 ± 2.2	2.0 ± 6.5	2.1 ± 5.5	1.8 ± 6.3
χ^2/NDF	$71.1/18$	$42.7/18$	$43.6/20$	$31.1/23$

$1 < \eta^* < 4$

W (GeV)	$80 \div 115$	$115 \div 150$	$150 \div 185$	$185 \div 220$
$\overline{n}$	6.41 ± 0.28	7.00 ± 0.39	7.52 ± 0.46	7.71 ± 0.30
$1/k$	0.085 ± 0.018	0.102 ± 0.014	0.132 ± 0.026	0.142 ± 0.020
χ^2/NDF	$96.8/21$	$112.4/21$	$88.6/25$	$44.7/24$
m	6.40 ± 0.33	6.98 ± 0.37	7.45 ± 0.41	7.59 ± 0.28
d	0.475 ± 0.009	0.484 ± 0.011	0.505 ± 0.023	0.527 ± 0.022
c	2.7 ± 1.3	2.7 ± 2.5	2.8 ± 7.1	4.5 ± 5.9
χ^2/NDF	$62.6/20$	$69.6/20$	$43.8/24$	$32.8/23$

$1 < \eta^* < 5$

W (GeV)	$80 \div 115$	$115 \div 150$	$150 \div 185$	$185 \div 220$
$\overline{n}$	6.90 ± 0.33	7.73 ± 0.41	8.44 ± 0.49	8.88 ± 0.34
$1/k$	0.067 ± 0.011	0.068 ± 0.012	0.074 ± 0.013	0.069 ± 0.020
χ^2/NDF	$44.7/19$	$57.0/21$	$80.8/24$	$63.6/25$
m	6.89 ± 0.29	7.72 ± 0.41	8.40 ± 0.48	8.78 ± 0.33
d	0.433 ± 0.010	0.422 ± 0.007	0.422 ± 0.015	0.422 ± 0.020
c	1.7 ± 1.5	1.8 ± 2.0	2.4 ± 5.1	4.1 ± 6.1
χ^2/NDF	$41.6/18$	$52.8/20$	$58.4/23$	$27.7/24$

Table 5: Parameters of Negative Binomial and Lognormal distributions in domains of pseudorapidity η^* and W. Errors quoted are the quadratic sum of the statistical error and systematic uncertainties.

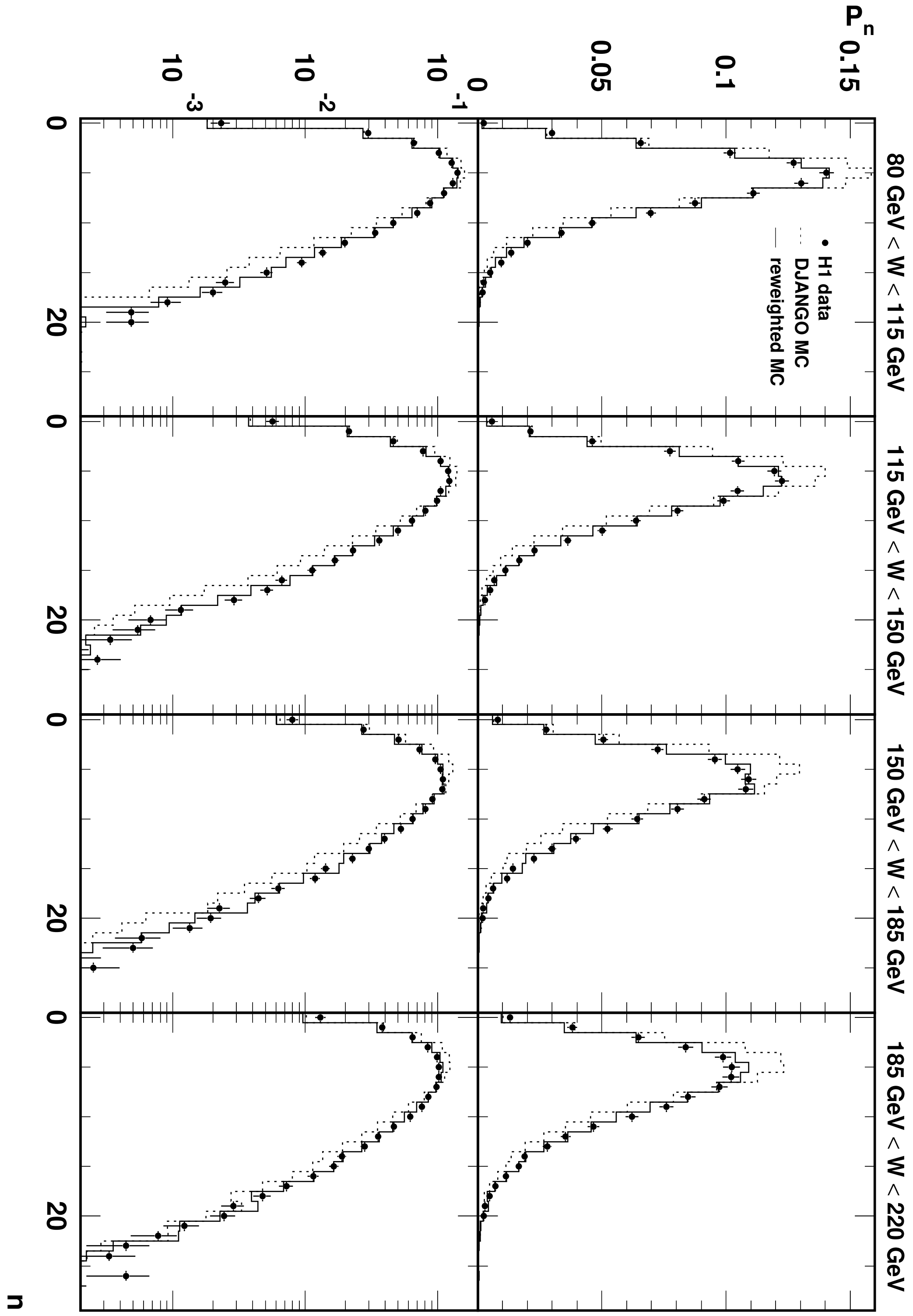

Figure 1: Raw data multiplicity distributions in the pseudorapidity range $1 < \eta^* < 5$ compared to DJANGO 6.0 and reweighted DJANGO 6.0 distributions, after detector simulation and reconstruction, in four W-regions.

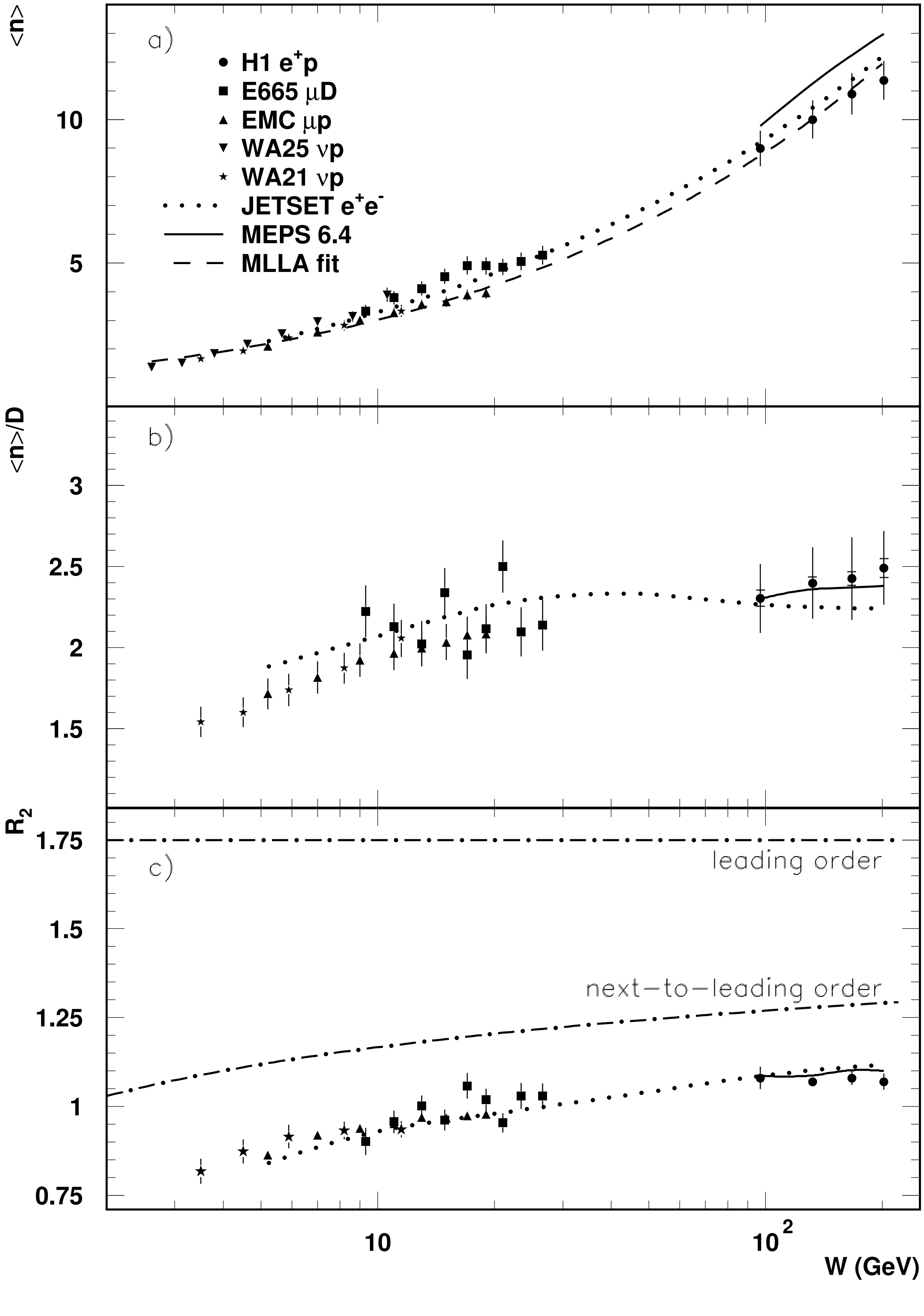

Figure 2: **(a)** W dependence of the mean charged particle multiplicity in the full current hemisphere in comparison with fixed-target lepton-nucleon data. The various curves are described in the text; **(b)** and **(c)** same as **(a)** for the ratio $\langle n \rangle / D$ and the second factorial moment R_2, respectively.

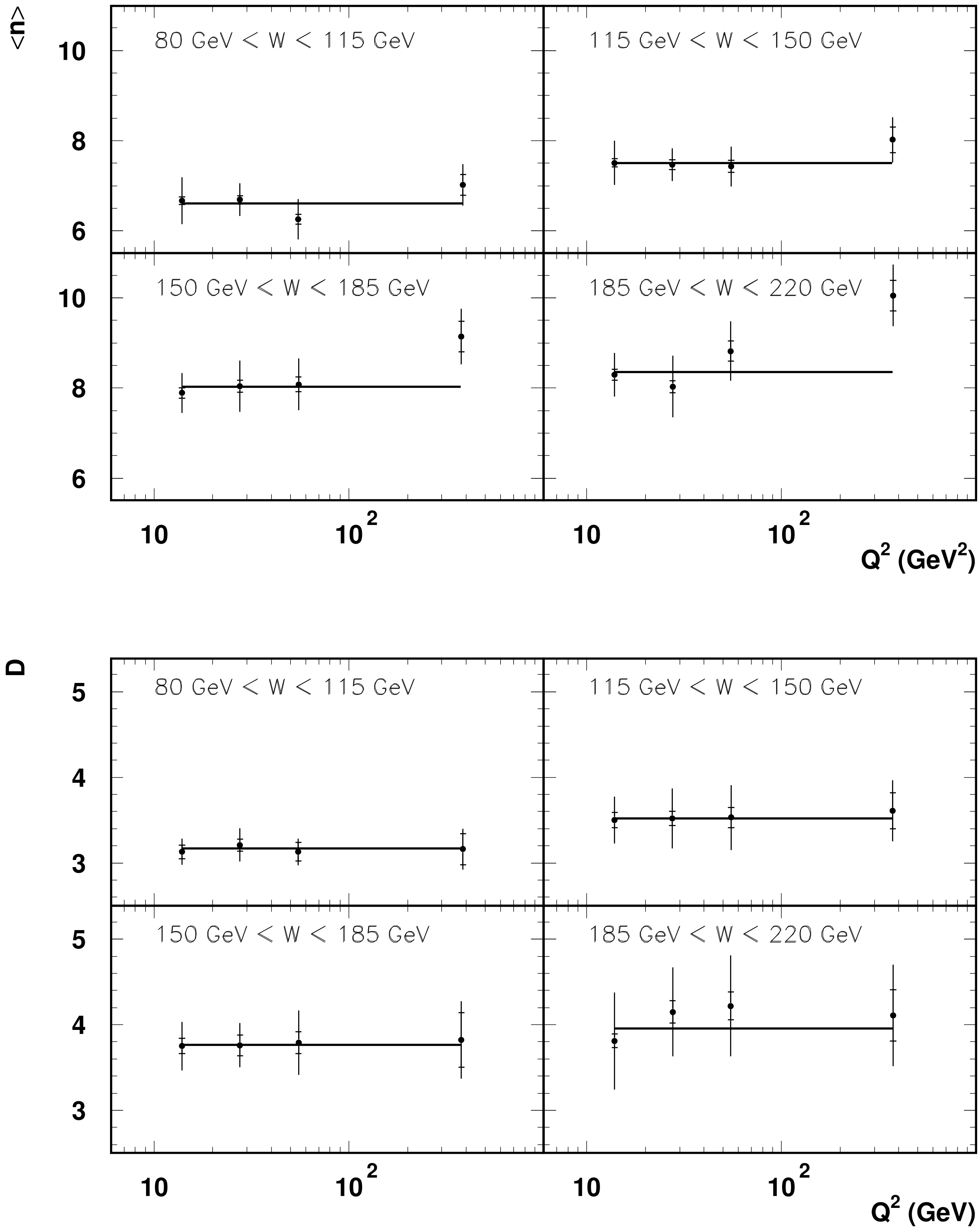

Figure 3: The Q^2 dependence of the mean charged particle multiplicity (top) and the dispersion (bottom) in intervals of W and in the domain $1 < \eta^* < 5$. Horizontal lines are fits to a constant. The inner error bars represent the statistical error, the outer error bars represent the total (quadratic sum of statistical and systematical) errors.

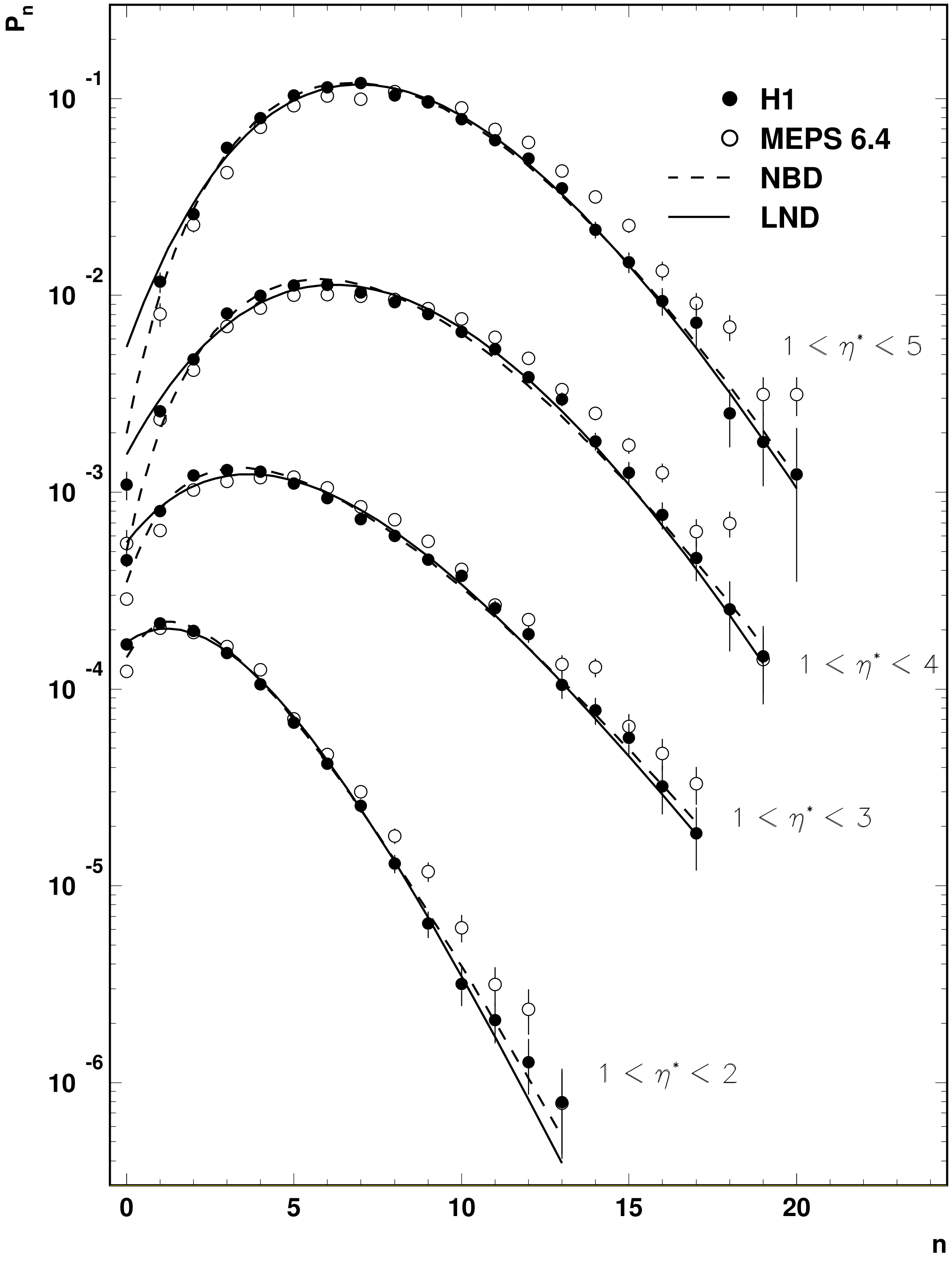

Figure 4: The unfolded multiplicity distribution in the interval 115 GeV $< W <$ 150 GeV and $Q^2 > 10$ GeV^2, in indicated pseudorapidity domains. The distribution for $1 < \eta^* < 5$ is plotted at its true scale; each consecutive distribution is shifted down by multiples of 10. The H1 data points (solid symbols) are compared to MEPS 6.4 (open symbols) and to fits with the Lognormal (full) and Negative Binomial (dashed) distribution. Statistical errors only are plotted.

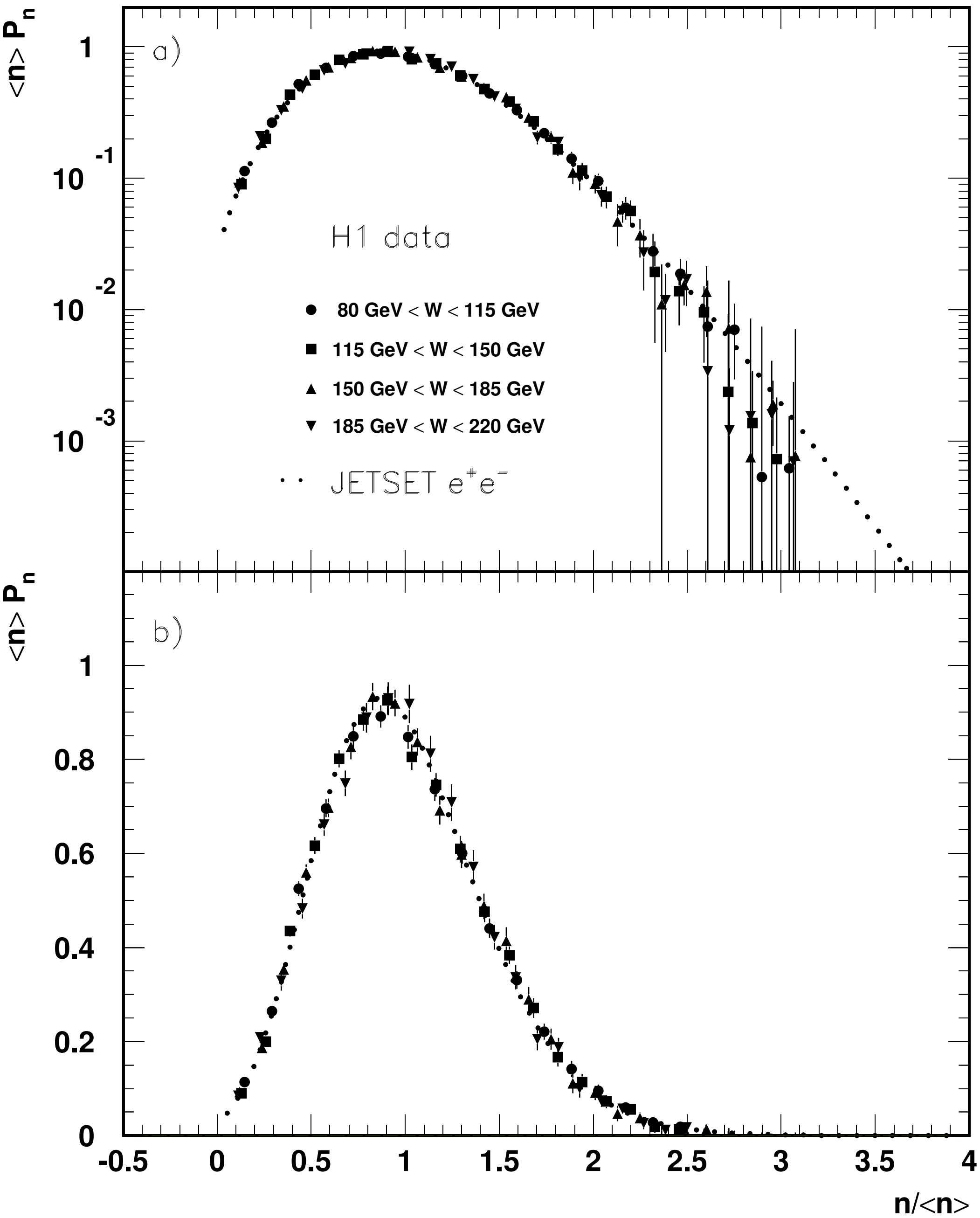

Figure 5: Unfolded multiplicity distributions in the pseudorapidity domain $1 < \eta^* < 5$ measured in different W intervals plotted in KNO-form, in logarithmic and linear scale. Statistical errors only are plotted.

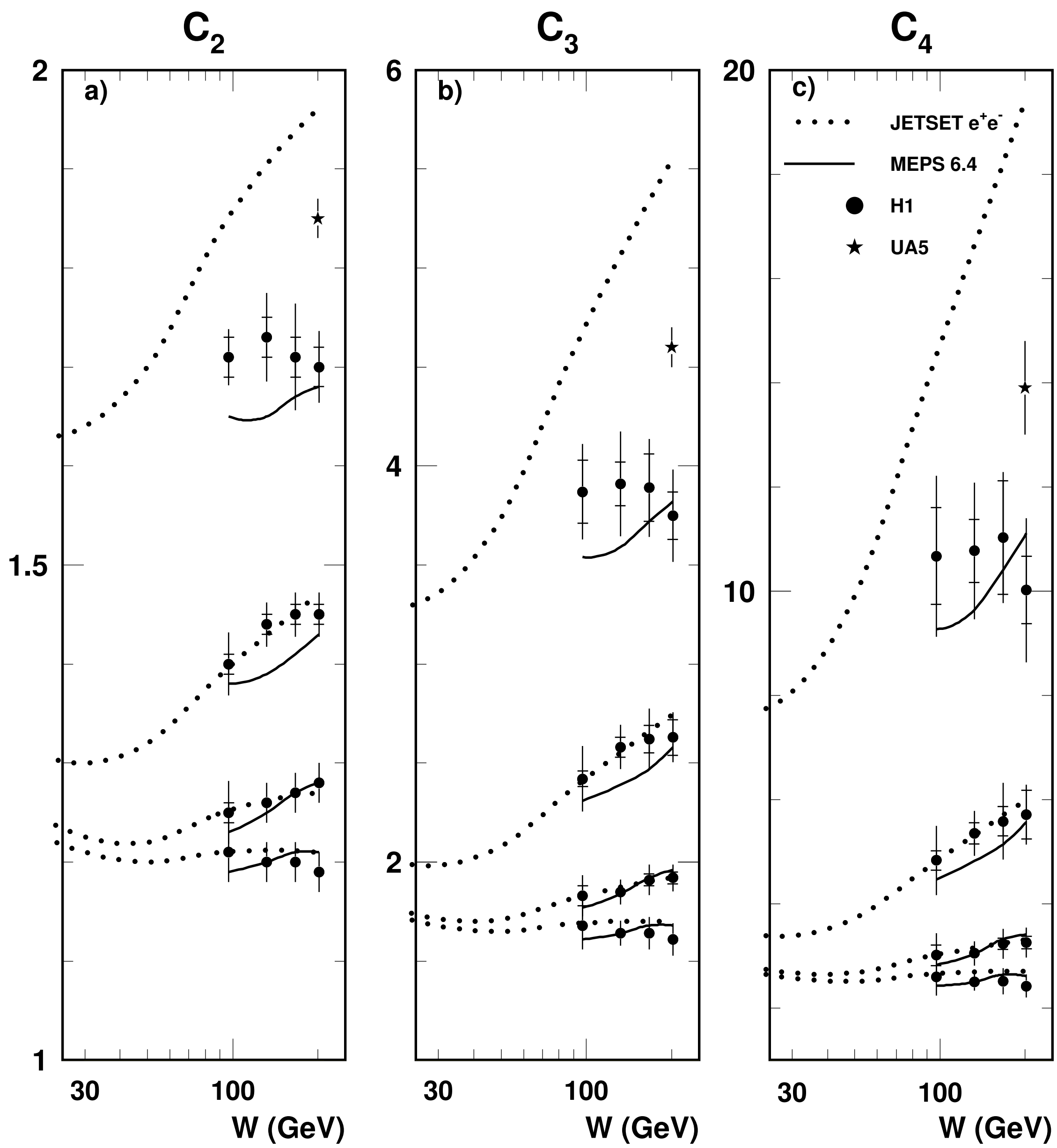

Figure 6: W-dependence of the multiplicity moments C_q in various η^*-domains. Data from UA5 [19] in the interval $1 < |\eta^*| < 2$ are also shown. From top to bottom, the domains are $1 < \eta^* < 2$, $1 < \eta^* < 3$, $1 < \eta^* < 4$ and $1 < \eta^* < 5$. The curves are described in the text. The inner error bars represent the statistical errors, the outer error bars represent the total (quadratic sum of statistical and systematical) errors.

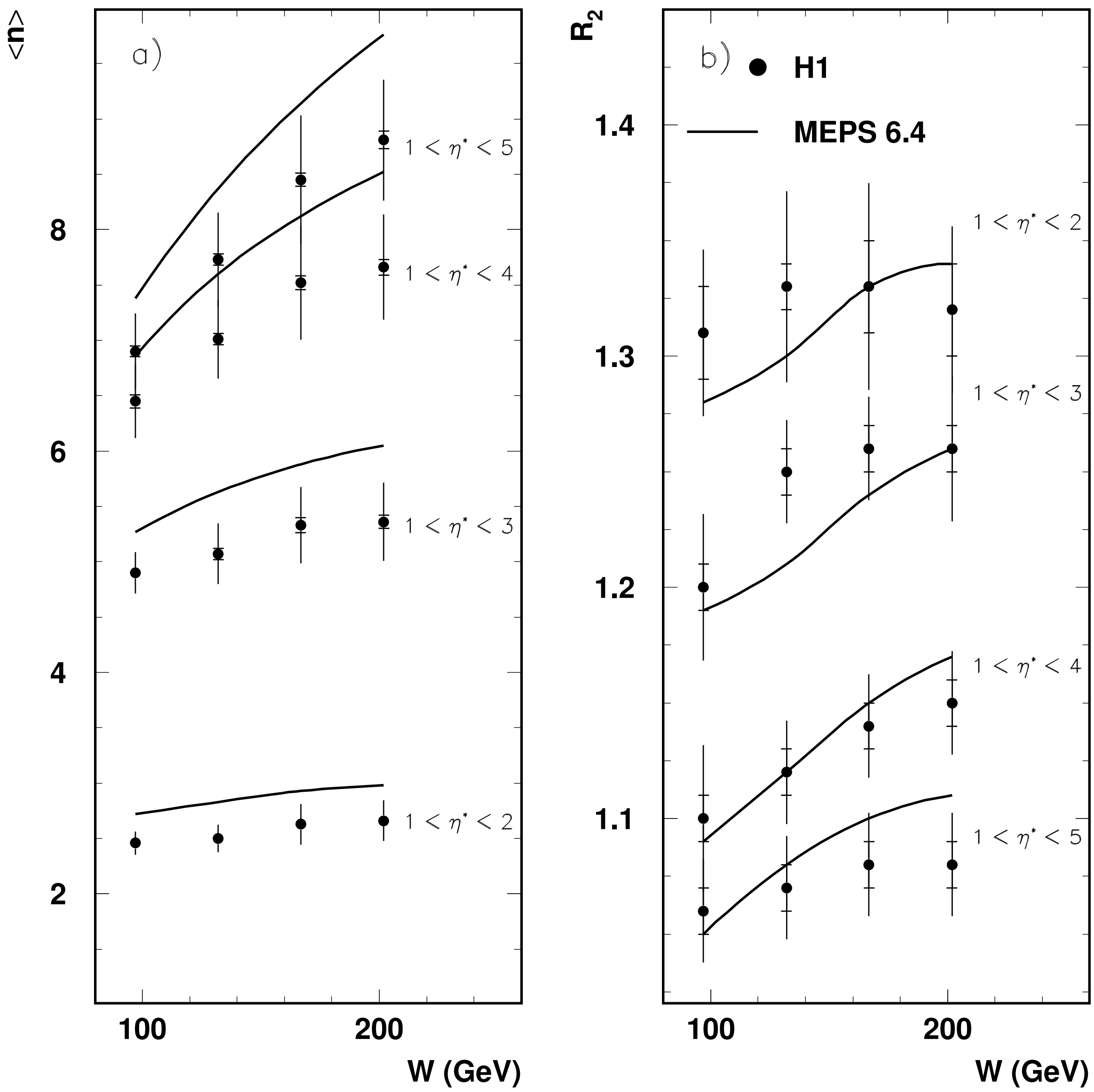

Figure 7: W-dependence of mean charged multiplicity and second-order factorial moment R_2 in indicated pseudorapidity domains, compared with MEPS 6.4 predictions. The inner error bars represent the statistical errors, the outer error bars represent the total (quadratic sum of statistical and systematical) errors.

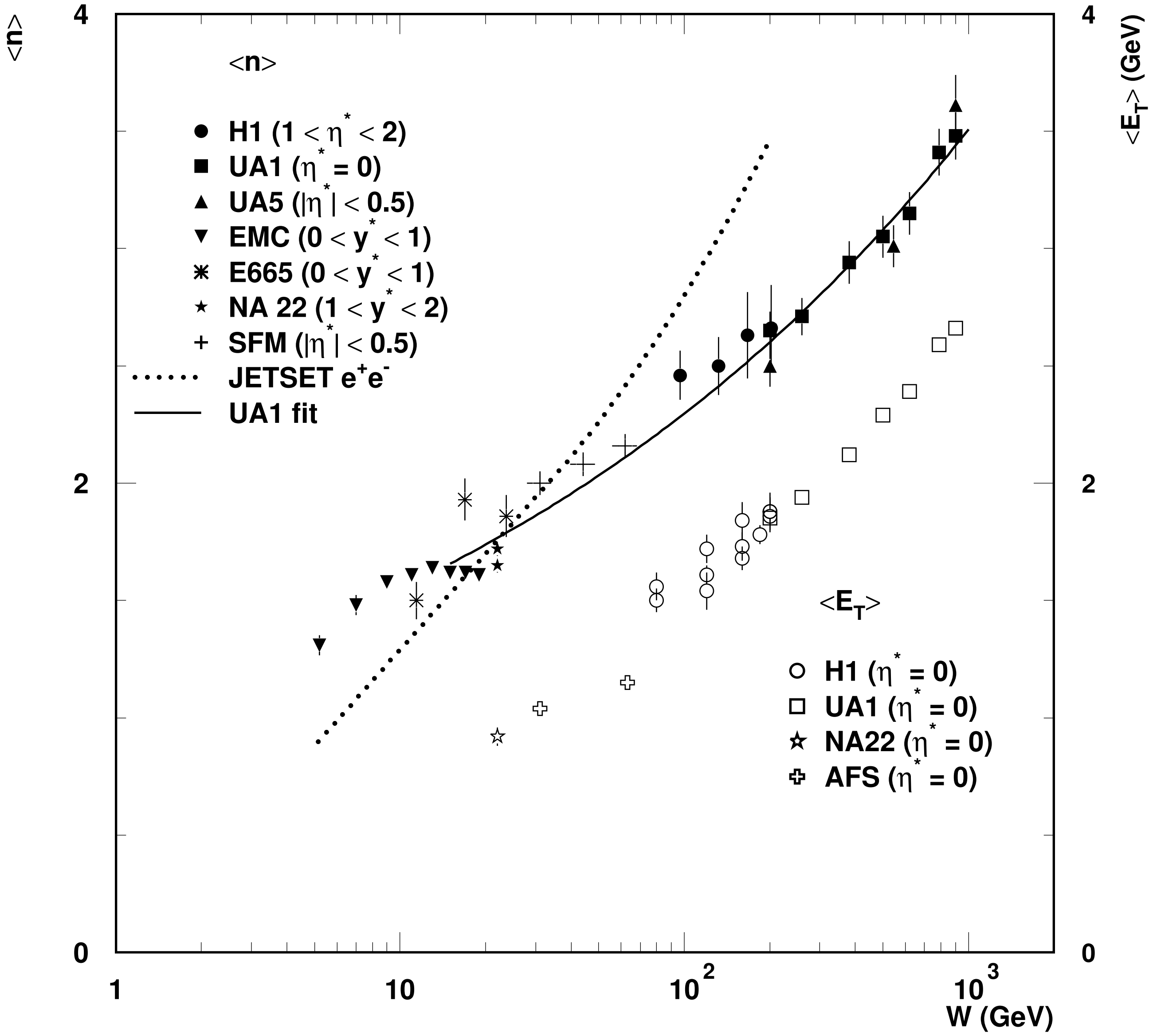

Figure 8: Solid symbols: W dependence of charged particle density in DIS and hadron-hadron collisions (left scale); open symbols: the mean transverse momentum flow, per unit of (pseudo)rapidity (right scale). The curves are described in the text. η^* is pseudorapidity, while y^* is rapidity in the hadronic centre-of-mass frame.